Polymer 50 (2009) 1067–1087

Contents lists available at ScienceDirect

Polymer

journal homepage: www.elsevier.com/locate/polymer

Feature Article

Transmission electron microtomography in polymer research

Hiroshi Jinnai [a,*], Richard J. Spontak [b,*]

[a] Department of Macromolecular Science and Engineering, Graduate School of Science and Engineering, Kyoto Institute of Technology, Kyoto 606-8585, Japan
[b] Departments of Chemical & Biomolecular Engineering and Materials Science & Engineering, North Carolina State University, Raleigh, NC 27695, USA

ARTICLE INFO

Article history:
Received 9 June 2008
Received in revised form
25 November 2008
Accepted 8 December 2008
Available online 24 December 2008

Keywords:
3D imaging
Transmission electron microtomography
3D digital image analysis
Block copolymers
Microphase-separated structures
Bicontinuous structures

ABSTRACT

This feature article summarizes recent advances in an emerging three-dimensional (3D) imaging technique, transmission electron microtomography (TEMT), and its applications to polymer-related materials, such as nanocomposites and block copolymer morphologies. With the recent developments made in TEMT, it is now possible to obtain *truly* quantitative 3D data with sub-nanometer resolution. A great deal of new structural information, which has never been obtained by conventional microscopy or various scattering methods, can be *directly* evaluated from the 3D volume data. It has also been demonstrated that, with the combination of TEMT and scattering methods, it becomes possible to study structures that have not yet been characterized. The structural information obtained from such 3D imaging provides a good opportunity not only to gain essential insight into the physics of self-assembling processes and the statistical mechanics of long chain molecules, but also to establish the "structure–property" relationship in polymeric materials.

1. Introduction

Polymer materials are ubiquitous in our daily life. They often consist of more than one species of polymers and thus become multi-component systems, such as polymer blends [1,2] and block copolymers [3]. Due to the repulsive interaction between the constituent polymers, the multi-component polymer materials often involve "phase-separation."

Studies to characterize such phase-separated structures inside materials have been significantly growing over the past couple of decades. Academic interest in complex fluids (to which polymeric systems belong) as well as a ceaseless industrial need for developing new materials has activated such studies. In academia, pattern formation and self-assembling processes of polymer blends are some of the most fascinating research themes for non-linear, non-equilibrium phenomena [4,5]. The block copolymers likewise self-organize (equilibrium) phase-separated nanometer-scale structures (termed "microphase-separated structures" in contrast to the "macrophase-separated structures" in the polymer blends). The block copolymers self-assemble microphase-separated structures due to the presence of chemical junctions inside the molecule; they cannot phase-separate on a micrometer scale because the constituent block chains are covalently connected. When phase-separated, they need to place their chemical junctions at the interface and the microdomain-forming blocks must uniformly fill the corresponding microdomains in the most entropically favored manner. Due to such constraints, the block copolymers normally form highly-periodic nano-structures. Thus, studies of the block copolymer morphologies belong to the statistical mechanics of long chain molecules. In industry, a deep understanding of such phase-separated polymer systems is also important in order to create nanomaterials with superior physical properties. The structure–property relationship in multi-component polymeric materials is of significant importance, i.e., basic studies of which eventually render the new design of polymer materials that satisfy the diverse requirements of industry.

Up to now, morphological studies of the multi-component polymeric materials have been carried out by various microscopic and scattering methods. Optical microscopes, transmission electron microscopes (TEMs), scanning electron microscopes (SEMs) and atomic force microscopes (AFMs) are commercially available and widely used. The biggest advantage of microscopy is that they provide intuitive real-space representations of the various morphologies. However, when it comes to "measurements", especially in a quantitative way, microscopy sometimes lacks a statistical accuracy due to the small field of view. In contrast, the scattering methods provide much a superior statistical accuracy than that of microscopy simply because the observation volume is larger than that of the microscopes. One must remember, however, that the scattering methods normally require "(hypothesized)

* Corresponding authors.
E-mail addresses: hjinnai@kit.ac.jp (H. Jinnai), spontak@ncsu.edu (R.J. Spontak).

0032-3861/$ – see front matter © 2008 Elsevier Ltd. All rights reserved.
doi:10.1016/j.polymer.2008.12.023

models" for data analysis in advance: They *do not* provide an intuitive insight into the morphologies as does microscopy. After all, for the complete characterization of a specific morphology, one may need to first know the morphologies from the microscopy and subsequently to evaluate the structural parameters by scattering on the basis of the morphology; the two methods are complementary.

Recently, phase-separated structures, especially the microphase-separated structures, are becoming increasingly complicated with advances in precision polymerization. Identification of such complex morphologies becomes more and more problematic. Micrographs taken by conventional microscopy, e.g., TEM, are often inconclusive. This makes the interpretation of the accompanying scattering data difficult. The conventional microscopes take two-dimensional (2D) (transmitted or surface) images of three-dimensional (3D) objects. The more complicated the morphologies, the less convincing the 2D images usually become. It is quite natural to develop new microscopes that are capable of obtaining 3D images.

Laser scanning confocal microscopy (LSCM) was developed in the 1980s and widely used first in the biological community for 3D direct observations of cell morphologies. After a slight delay, it has become popular in the materials community. In the polymer society, LSCM was first used to observe the bicontinuous morphology of a polymer mixture during spinodal decomposition [4–6]. X-ray computerized tomography (X-ray CT) is another technique for 3D imaging that has a similar spatial resolution, but not better than a few micrometers. The biggest advantage of X-ray CT to LSCM is the strong penetrative power of the X-ray so that it can be readily used for opaque materials. At the opposite end of the resolution scale, the atom probe field ion microscope (APFIM) has been developed to allow atom probe tomography to be undertaken with true atomic scale accuracy [7]. Although it is the only one that allows single atom counting of a 3D structure, the sample needs to be conducting and withstand high field stresses exerted at the tip of the needle-shaped sample necessary for APFIM. Thus, generally speaking, APFIM is not so suitable method for soft materials, such as polymers.

There seems to be a need for another technique to fill this middle ground that offers an intermediate resolution (of about 1 nm) with a field of view of hundreds of nm, making it ideal for the characterization of many polymeric structures. Transmission electron microtomography (TEMT) is an emerging technique for the 3D structural observations in polymer nanotechnology. Although the first paper using TEMT appeared in *Polymer* as early as 1988 by Spontak et al. [8], it has not been extensively used until recently by the scientific community due to various reasons that will described later in more detail. In the new millennium, TEMT is becoming more frequently used by several groups around the world to investigate block copolymer morphologies. The highest resolution of TEMT to date is ca. 0.5 nm [9,10].

In the present feature article, we focus on the 3D structural observations and analysis of polymer nano-structures using TEMT. This article is organized in the following way: In Sections 2 and 3, we describe the basics and some recent developments of TEMT, respectively. In Section 4, some examples of the TEMT of polymer-related structures will be introduced. In Sections 4.1 and 4.2, examples of the structural characterizations of two kinds of nanocomposite materials will be presented. Applications of TEMT to block copolymer morphologies will be shown in Section 4.3. As mentioned above, microscopy (real space measurement) and scattering (reciprocal space measurements) are complementary. In Section 5, TEMT was used together with neutron reflectivity to investigate the microphase-separated structure in a block copolymer thin film. By combining the two methods, a complete picture of the internal morphology was obtained.

2. Some basics of electron tomography

The need to obtain a higher dimensional "structure" using lower dimensionality data is present in many different fields of the physical and life sciences. The first application of this idea appeared in the field of astronomy [11]. They proposed a method of reconstructing a 2D map of solar microwave emissions from a series of 1D radio telescope data. In 1963, a possible application in medicine stimulated interest in tomographic reconstruction [12]. The development of the X-ray computed tomography scanner was based on Cormack's work [13], which led to a joint Nobel Prize for Cormack and Hounsfield in 1979. This is the most well-known application of the 3D tomographic reconstruction. The first tomographic reconstruction from electron micrographs can be found as early as 1968 [14–16], which was followed by a number of theoretical papers discussing the theoretical limits of Fourier techniques [17], approaches to real space reconstruction [18,19] and iterative reconstruction routines [20,21].

While the theory rapidly advanced, the experimental results were slow to appear. The limiting factors are beam damage, the poor performance of goniometers and computing power for image processing and reconstruction. The last two factors of electron tomography are no longer problems, but the beam damage is still the limiting factor for most of the polymer samples. In the biological sciences, the samples are cooled to liquid helium temperature under high voltages to reduce the beam damage, thus electron tomography in this area has developed to the point where the reconstruction of objects is possible with a resolution of 2 nm [22].

It was Radon who first outlined the mathematical principles behind tomography in 1917 [23], in which he defined the *Radon transform*. It shows the relation between a function, $f(x, y)$, describing a real space object, and its projection (or line integral), $p(r, \theta)$, through f along all possible lines B with unit length ds:

$$p(r,\theta) = \int_B f(x,y)\mathrm{d}s. \tag{1}$$

The geometry of the Radon transform is displayed in Fig. 1(a). The sampling of an experimental object by some forms of transmitted signal or projection is geometrically equivalent to a discrete sampling of the Radon transform. Thus, the reconstruction of the structure of the object $f(x, y)$ from the projections $p(r, \theta)$ can be achieved by the implementation of the inverse Radon transform.

In practice, the reconstruction from projections is aided by an understanding of the relationship between an object and its projections in the Fourier space; "the central slice theorem" [13,24] states that the Fourier transform of an object's projection is a central plane in the Fourier transform of the object as shown in Fig. 1. The Fourier transform of $p(r, \theta)$ is:

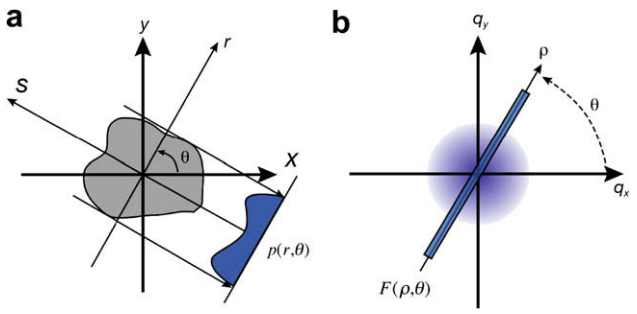

Fig. 1. The discrete form of the central slice theorem in 2D. A projection $p(r, \theta)$ in real space (x, y) at angle θ is a slice $F(\rho, \theta)$ at the same angle in the Fourier space (q_x, q_y).

$$F(\rho,\theta) = \int_{-\infty}^{\infty} p(r,\theta)\mathrm{e}^{-\mathrm{i}\rho r}\mathrm{d}r. \quad (2)$$

where q is the wavenumber. The Fourier coefficients, $F(\rho, \theta)$, are arranged along the line in the Fourier space with the same tilting angle θ. Thus, a projection taken by the TEM will equate to part of an object's Fourier transform, sampling the object over the full range of frequencies in a central section. Although the shape of most objects will be only partially described by the frequencies in one section, many sections will be sampled in the Fourier space if a sufficiently large number of projections are taken over as wide a tilting range as possible. Therefore, tomographic reconstruction is possible from an inverse Fourier transform of $F(\rho, \theta)$. This is known as the *direct Fourier reconstruction* [25,26].

$$f(x,y) = \int_{-\infty}^{\infty}\int_{-\infty}^{\infty} F(q,\theta)\mathrm{e}^{\mathrm{i}\rho(x\cos\theta+y\sin\theta)}\rho\mathrm{d}\rho\mathrm{d}\theta. \quad (3)$$

This Fourier space reconstruction approach is, in practical use, not very easy. This is because the projection data is always sampled at discrete angles leaving regular gaps in the Fourier space. The inverse Fourier transform intrinsically requires a continuous function, and therefore, radial interpolation is required to fill the gaps in the Fourier space. Thus, the quality of the reconstruction is significantly affected by the type of implemented interpolation [27].

The faster and easier (and thus most commonly used) algorithm (than the direct Fourier reconstruction) is the *back-projection* method [28]. This method relies on the following simple reasoning: a point in space may be uniquely described by any three rays passing through the point. If the object becomes increasingly complicated, more rays are then necessary to uniquely describe it. The projection that can be obtained from TEM is essentially an inversion of such a ray, and describes some of the complexity of the object. Therefore, inverting the projection generates a ray that will uniquely describe an object in the projection direction; this is called *back-projection*. The superposition of the back-projected rays from different angles will return the shape of the original object. This is a technique known as *direct back-projection* [15,17,29] detailed algorithms of which can be found in the literature [26,29]. In practical use, however, the reconstructions by the back-projection method are often blurred due to the uneven sampling of the spatial frequencies in the ensemble of the original projections. Namely, sampling density near the center of the Fourier space is greater than that in the periphery. In order to correct such a sampling imbalance, a simple weighting filter (a radially linear function in the Fourier space, zero at the center and a maximum at the edge) is multiplied by the reconstruction in the Fourier space. This is known as *weighted back-projection* (WBP) [17,30].

In the case of TEMT, the projections at different angles are collected by tilting the specimen with respect to the electron beam in the TEM column. The achievable tilt range in a TEM is restricted by the relative geometries of the specimen holder and objective lens because they will physically contact at a high tilt angle, e.g., 70°. The missing information due to this limitation becomes a wedge-shaped region in the Fourier space, i.e., *the missing wedge*, giving rise to a loss of resolution for the reconstructed image especially in the direction parallel to the electron beam. Although the restoration of the missing structural information has been studied [31], the fundamental solution of which may be difficult. Some of the experimental challenges to solve (or reduce) the missing wedge will be presented in Section 3.

During tilting the specimen, misalignments in the digitized images are also inevitable due to the imperfect eccentricity of the specimen stage. As a crucial prelude to calculating a 3D reconstruction, alignment of the digitized images is necessary. This is achieved either by the least squares tracking of fiducial markers [32], such as small gold particles, or by sequential cross-correlation. Often a combination of both processes is used [22]. For readers who want to know the technical sides of TEMT in more detail, there are an excellent book [32] and some review papers [33,34].

3. Recent development in transmission electron microtomography (TEMT)

As mentioned above, an intrinsic limitation of the angular range for the tilting experiment available with TEM results in the missing wedge of structural information in the Fourier space. Due to the missing wedge, resolution along the direction parallel to the optical axis of the microscope (the dimension perpendicular to the plane of the specimen), i.e., the *Z*-direction, is reduced compared to that in the specimen plane [35]. In addition to this primary effect, a less appreciated, but probably critical effect of the missing wedge is that the appearance in the 3D reconstruction of elongated objects in the specimen plane strongly depends on their angle relative to the tilt axis. This effect will be detailed in a later section (Section 3.1.1). Although the cylindrical and lamellar morphologies of the block copolymers could be influenced by the latter effect in the TEMT observations, few of the previous studies dealing with such anisotropic nano-structures [8] considered the effect.

3.1. Dual-axis TEMT

3.1.1. A problem in a single-axis TEMT: the "missing wedge" problem

Fig. 2 shows a simulation of the single-axis TEMT for cylindrical morphologies. As shown in Fig. 2(a)–(c), three different geometries of the cylinders with respect to the tilt axis and orientation were simulated. In these figures, the hexagonally packed cylinders orient in three different directions while the tilt axis is fixed in the *X*-direction. The cylinders were tilted around the tilt axis typically from −60° to 60° in an increment of 1°, from which the WBP method [17,30] was used to obtain tomograms. Fig. 2(d)–(l) displays cross-sectional images of the 3D reconstruction. In the *Y*–*Z* plane, the cross-sections (d) and (f) that correspond to the models (a) and (c) were properly reproduced. On the other hand, the cross-section (e) from the model (b) was poorly reconstructed; the horizontal stripes should be observed. Fig. 2(g)–(i) and Fig. 2(j)–2(l) show, respectively, the *X*–*Z* and *X*–*Y* planes. Although the cross-sections relevant to the models (a) and (c) were obtained with a reasonable accuracy, again, the cross-sections corresponding to model (b) [see Fig. 2(h)–(k)] were not correctly reconstructed. In fact, judging only from the cross-sectional images obtained from model (b), i.e., Fig. 2(e), (h) and (k), one could misidentify the 3D structure with the lamellar morphology whose lamellar normal in aligned to the *X*-axis. Thus, if the orientation of the cylindrical nanodomains geometrically satisfies the relation with the tilt axis as shown in Fig. 2(b), it is very likely that the cylinders *do not* appear in the 3D reconstruction.

This problem can be understood by considering the relationship between a projection in the real space and the Fourier space. If some projections are missing due to the limited angular range of the TEM, then the Fourier space is under-sampled in those directions. The unsampled volume in the Fourier space becomes wedge-shaped. Fig. 2(m)–(o) demonstrates the missing wedge in the Fourier space (translucent gray volume) and "diffraction patterns" of the cylindrical microdomains relevant to the geometries shown in Fig. 2(a)–(c), respectively. Although the tilt axis lies along the same direction, the *X*-direction, in all models, the orientation of the cylinders is different and hence the diffraction spots of the cylindrical microdomains appear differently. In the case of Fig. 2(m)–(o),

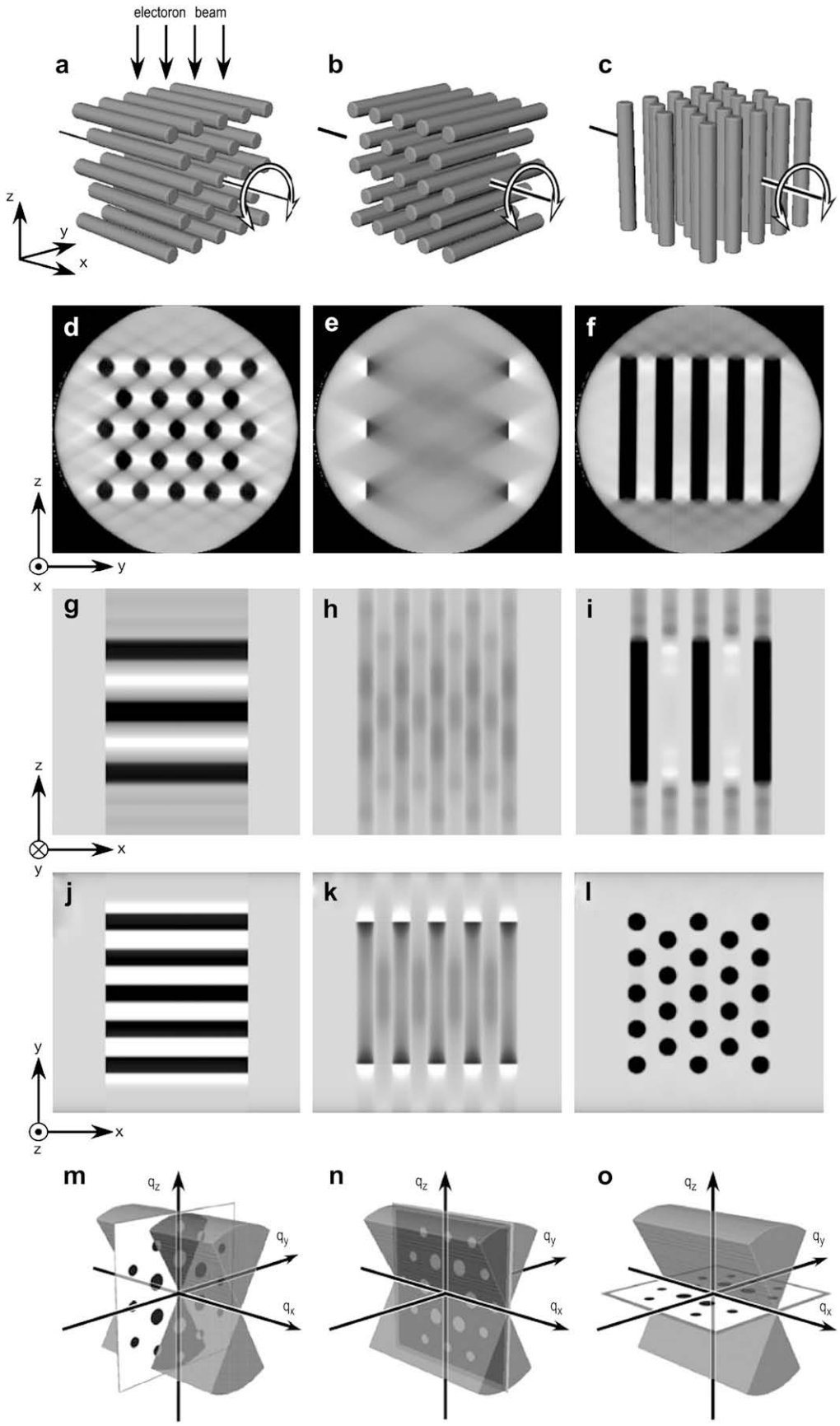
electoron beam
a
b
c
z
y
x
d
e
f
z
y
x
g
h
i
z
x
y
j
k
l
y
x
z
m
n
o
q_z
q_y
q_x

part of and all of the diffraction spots are outside the missing wedge, and hence, it is feasible to obtain reasonable 3D reconstructions. In fact, the image quality of the 3D reconstruction of model (c) appears to be the best among the three geometries [see Fig. 2(l) for example]. On the other hand, all the diffraction spots are inside the missing wedge in Fig. 2(h), resulting in an insufficient 3D reconstruction.

One of the most effective ways to solve this problem is to minimize the volume of the missing wedge. Increasing the tilting angle of the specimen may be one possible way, however, this strategy would not significantly help especially in the case of the 3D observation of a cylindrical morphology as demonstrated in Fig. 2(b). Another strategy is to have another tilt axis in addition to the first one. Fig. 3 demonstrates such a "dual-axis tomography." In Fig. 3(a) the unsampled volume of the dual-axis tomography is shown. Compared with the missing wedge shown in Fig. 3(b) [that is the reproduction of Fig. 2(n)], the unsampled volume in the dual-axis tomography, called the "missing pyramid", becomes *considerably* smaller than the missing wedge. Some of the diffraction spots of the cylindrical nanodomains are now outside the missing pyramid even in the case of the geometry shown in Fig. 2(b), indicating that the cylinders would be reconstructed. Penczek et al. [36] pioneered the dual-axis tomography for thick biological sections, followed by Mastronarde [37].

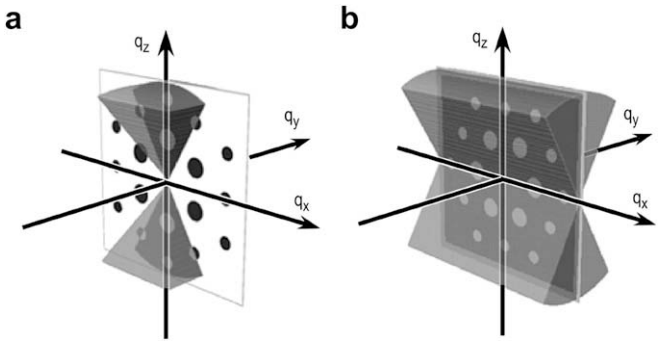

Fig. 3. Comparison of the missing volume in the Fourier space between (a) the dual-axis tomography and (b) the single-axis tomography. Directions of the tilt axes in the dual-axis tomography are along the q_x and q_y axes. In the single-axis tomography, the tilt axis is along the q_x axis. The hexagonally packed infinitely-long cylindrical morphology aligned along the *Y* axis as shown in Fig. 2(b) gives a diffraction pattern only in the q_x–q_z plane. Some of the diffraction spots are outside the "missing pyramid" and hence the cylinders can be reconstructed in the dual-axis tomography [part (a)], while all the diffraction spots are inside the "missing wedge" in the single-axis tomography [part (b)]. Reproduced with permission from Ref. [35]. Copyright 2005 American Chemical Society.

3.1.2. Dual-axis TEMT on a cylindrical microphase-separated structure

Fig. 4 shows the results of the 3D reconstruction of a poly (styrene-*block*-isoprene) (SI) copolymer. The number-averaged molecular weight and polydispersity index are $M_n = 5.1 \times 10^4$ and $M_w/M_n = 1.06$, respectively. The isoprene volume fraction, f_I, was 0.22. A specimen film was prepared by spin coating from a toluene solution of the SI copolymer onto a mica substrate. The copolymer film on the substrate was further annealed. It was then floated off the mica substrate and placed on a Cu mesh grid. The film was stained with OsO_4 vapor. Additional experimental details can be found elsewhere [35].

Fig. 4(a) and (b) displays, respectively, the orthogonal views of the two 3D reconstructed volume data with the tilt axes in different directions, i.e., the *Y*- and *X*-directions. The solid and dashed lines in each cross-sectional slice represent the positions of the other two orthogonal slices. The thickness of each digitally sliced cross-section in Fig. 4(a) and (b) is equal to the edge length of a voxel, i.e., 1.9 nm. These images were *outstandingly* clear due to essentially no overlap of the nano-structure. The cross-sectional slice is called as "digital slice" throughout this paper. We note here that one of the biggest advantages of TEMT is that it obtains true 3D information on intact block copolymer morphology by digital sectioning, instead of physically cutting the materials into slices.

In Fig. 4(a) and (b), the two 3D reconstructions show exactly the same volume of the specimen except for the direction of the tilt axis. It is clear that the SI block copolymer exhibited a PI cylindrical morphology. The cylinders lay parallel to the film surface. The thickness of the film was determined to be ca. 160 nm from cross-sections in the *X*–*Z* plane in Fig. 4(a) and the *Y*–*Z* plane in Fig. 4(b). It was found that there were 6 layers of cylindrical nanodomains in the film as observed from the *X*–*Z* plane in Fig. 4(a) and the *Y*–*Z* plane in Fig. 4(b).

It is quite intriguing that some parts of the 3D reconstruction either in Fig. 4(a) or in Fig. 4(b) were not properly reconstructed. For example, the horizontally oriented cylinders shown by a circle in the *X*–*Y* plane of Fig. 4(a) were only slightly visible, while they were *clearly* visible in the *X*–*Y* plane of Fig. 4(b). As described earlier, the cylinders in this area fulfilled the geometrical relation as shown in Fig. 2(b), and hence they were not properly reconstructed in Fig. 4(a). On the other hand, the same cylinders were parallel to the tilt axis (*X*-axis) in Fig. 4(b), corresponding to the situation shown in Fig. 2(a). Thus, they were successfully reconstructed.

The interface between the PI and PS nanodomains was found by binarizing the morphologies in the *X*–*Y* plane and was modeled according to the marching cubes algorithm (MCA) [38]. Fig. 4(c) and (d) shows the surface-rendered 3D images of the SI block copolymer corresponding to those displayed in Fig. 4(a) and (b), respectively. The tilt axes are indicated by rods. The volume fraction of the PI microdomains evaluated from Fig. 4(c) and (d) was, respectively, 0.16 and 0.15, contrary to the known composition of the copolymer, 0.22.

The two 3D reconstructed data at the same position of the specimen were combined in the Fourier space, the detailed protocol of which can be found elsewhere [35]. Orthogonal views of the combined 3D reconstruction are displayed in Fig. 5(a) together with a corresponding surface-rendered 3D image in Fig. 5(b). Because the positions of the orthogonal views in Fig. 5(a) are exactly the same as those in Fig. 4(a) and (b), it is now obvious how much the dual-axis tomography can improve the single-axis 3D reconstructions; not only in the lateral plane (*X*–*Y* plane), but also in the cross-sectional planes, i.e., the *X*–*Z* and *Y*–*Z* planes, cylindrical microdomains were visible regardless of their orientations. The volume fraction of the PI domains evaluated from the surface-rendered image was ca. 0.22. This result indicates that the dual-axis tomography should be used to obtain quantitative 3D data, if the nano-structure is highly anisotropic.

Fig. 2. Demonstration of the effect of the geometrical relationship between the direction of the tilt axis and the orientation of cylindrical nanodomains on the 3D reconstruction. There are three types of geometrical relationships. Each column shows a model, three cross-sections of the 3D reconstruction and a "missing wedge" in the Fourier space (shown by the gray volume), from top to the bottom. The cylindrical nanodomains rotate around the tilt axis from -60° to 60° with a 1° increment. The tilt axis is always along the *X*-direction. The electron beam comes from the top (from the *Z*-direction). An *X*–*Z* cross-section is a tomogram where WBP is carried out. In the bottom-most row, diffraction patterns from the infinitely-long cylinders are shown together with the missing wedge. Because the missing wedge is the volume in the Fourier space where no projections can be sampled, diffraction spots within this wedge cannot contribute to the resulting 3D reconstruction. Reproduced with permission from Ref. [35]. Copyright 2005 American Chemical Society.

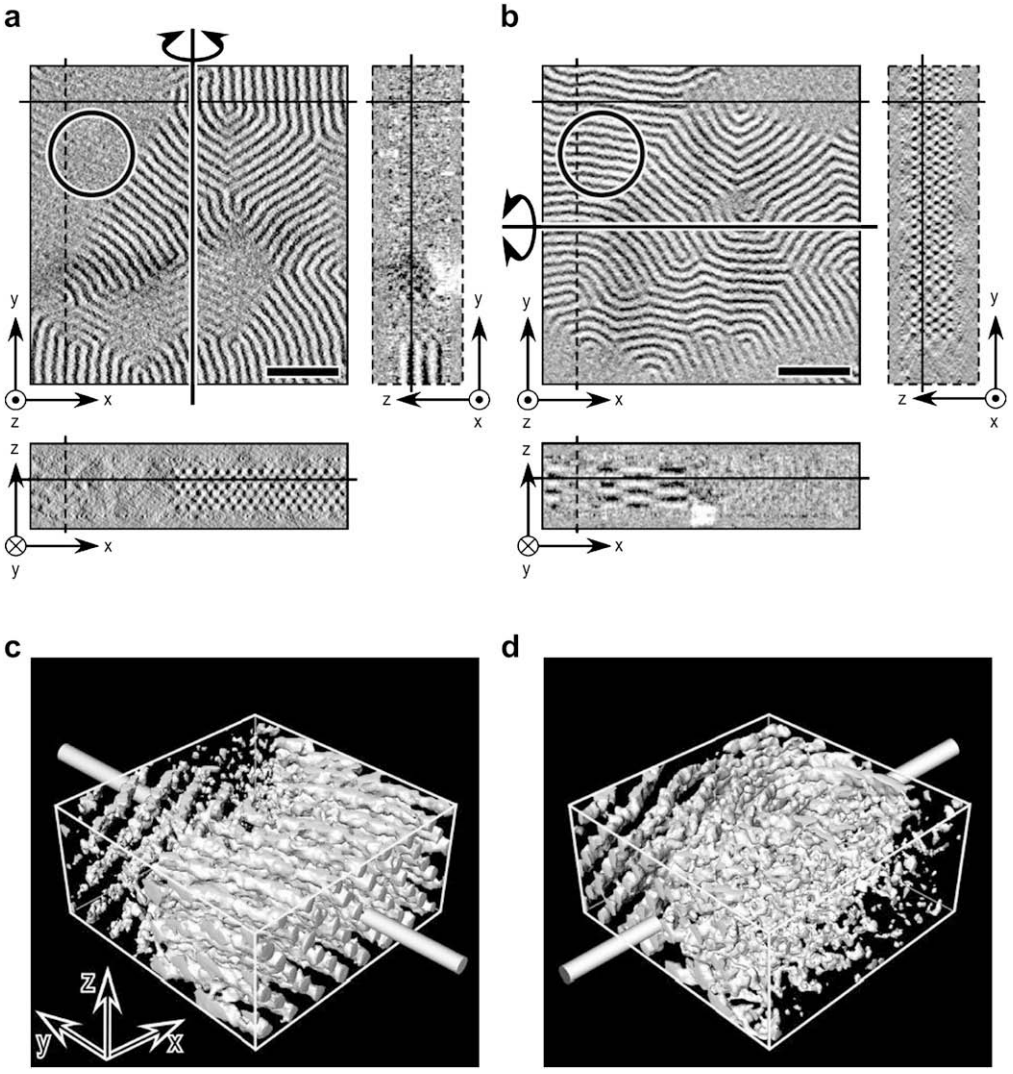

Fig. 4. Orthogonal cross-sectional views of (a) *Reconstruction 1* and (b) *Reconstruction 2*. The tilt axes lie along (a) *Y*- and (b) *X*-directions, respectively. In parts (a) and (b), as indicated by the circles, some cylindrical nanodomains were not reproduced in part (a), but were nicely reconstructed in part (b) and vice versa. The solid and dashed lines in the cross-sections represent positions where each slice was cut in the 3D reconstructed data. Parts (c) and (d) show the surface-rendered 3D images, where the PS region has been made transparent. The tilt axes are indicated by the solid rods. The scale bar in parts (a) and (b) shows 200 nm. The box size of the 3D image is 250 nm × 250 nm × 115 nm. Reproduced with permission from Ref. [35]. Copyright 2005 American Chemical Society.

3.2. TEMT without "missing wedge"

In the previous section, the dual-axis TEMT was introduced in order to reduce the missing wedge in the TEMT. Although the missing region in the Fourier space can be significantly reduced by the dual-axis TEMT, the more successful tactic for the CT is to tilt the specimen over ±90°. In this section, we demonstrate the complete rotation of a rod-shaped specimen of a zirconia/polymer nanocomposite made by the focused ion beam (FIB) method that was attached to the tip of a specially modified specimen holder without any supporting film. A complete set of tomograms has been generated from 181 projections that were taken over the angular range of ±90° [9].

Fig. 6(a) shows an electron micrograph of the rod-shaped specimen. The 5–20 nm zirconia grains were observed as black domains in the polymer matrix in the enlarged electron micrograph [Fig. 6(b)]. No sign of damage occurred during the FIB fabrication process, such as melting by the gallium ion beam or the re-deposition of contaminates, was observed on the surface of the rod-shaped specimen. Note that the applicability of the FIB to polymer materials has also been confirmed on an SI block copolymer [39].

An orthogonal view of the reconstructed 3D image of the zirconia/polymer nanocomposite is shown in Fig. 7. The gray region and white small objects are, respectively, the thermoset polymer matrix and zirconia domains. The conventional TEMT in which the angular range is limited to ±60° shows artifacts at the top and bottom of the *X*–*Z* plane, and the objects are elongated along the *Z*-axis [see Fig. 8] [40]. It is quite impressive that the 3D reconstruction of the nanocomposite is totally free from such artifacts. Moreover, the *Y*–*Z* plane, which usually exhibits the worst image quality in the conventional TEMT, appeared as clear as the other two cross-sectional slices.

Image artifacts due to limitations of the angular range prominently appear in the *X*–*Z* plane. Because we have the complete data set with ±90° angular tilting, it is worthwhile to demonstrate how the maximum tilt angle affects the image quality and resolution in the TEMT experiments. A series of 3D reconstructions with various

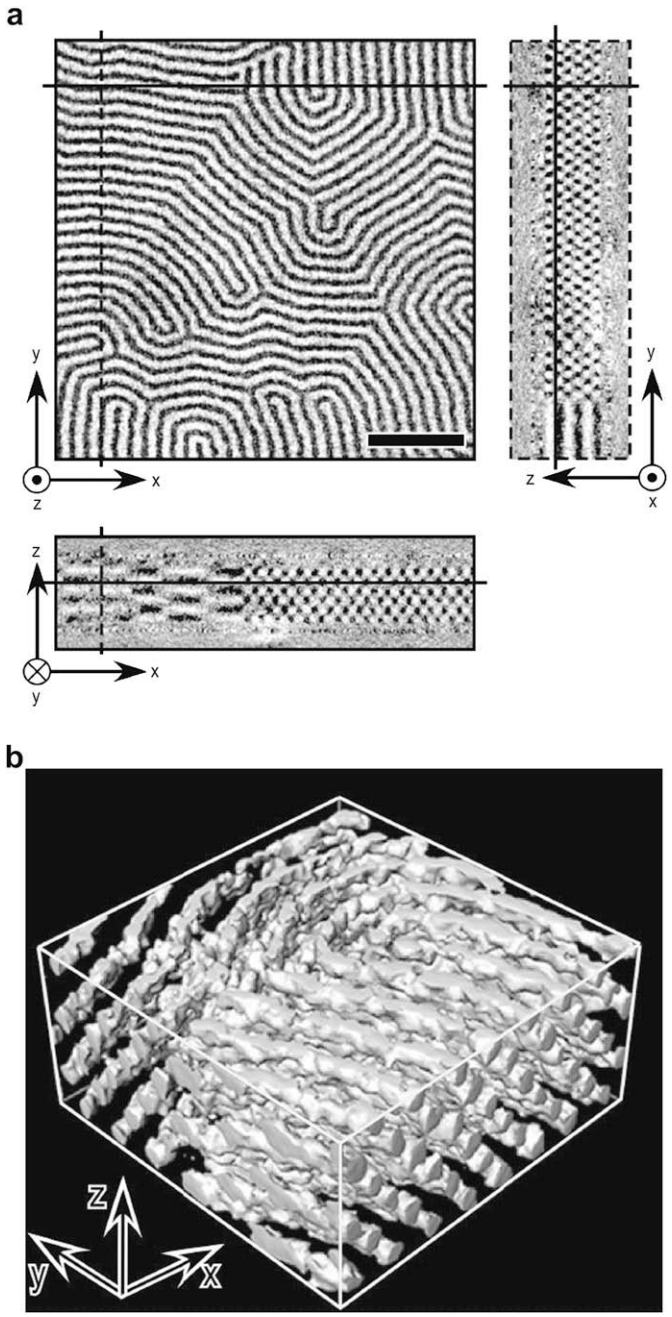

Fig. 5. (a) Orthogonal cross-sectional views of 3D reconstructions obtained from dual-axis tomography. Positions of the cross-sections are exactly the same as those in Fig. 4. The black phase is The PI nanodomain. The cylindrical nanodomains are completely reconstructed not only in the *X*–*Y* plane, but also in the other two orthogonal cross-sections. The scale bar shows 200 nm. (b) Surface-rendered 3D images obtained from dual-axis tomography, where the PS region has been made transparent. Box size of the 3D image is 250 nm × 250 nm × 115 nm. Reproduced with permission from Ref. [35]. Copyright 2005 American Chemical Society.

maximum tilt angles, α, were made. Namely, the 3D images were reconstructed from exactly the same TEM tilt series and alignment within the angular range of $\pm\alpha^{\circ}$. Fig. 8(a) shows the *X*–*Z* cross-sections of the same region of the rod-shaped specimen from $\alpha = 40^{\circ}$ to $\alpha = 90^{\circ}$ in 5° increments. As α decreased, the image quality, especially the contrast between the zirconia grains and polymer matrix, became worse, and also the edge of the rod-shaped specimen became more like a "pear-shape" rather than the rod-shape. Note that the angular range is normally limited to

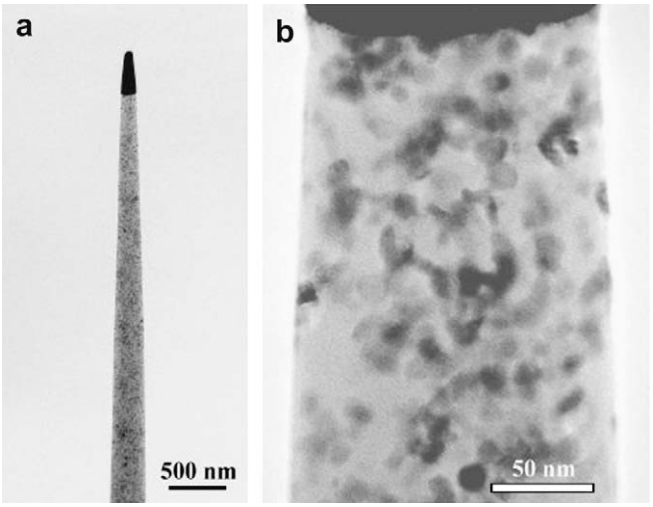

Fig. 6. (a) An electron micrograph of a rod-shaped polymer nanocomposite containing zirconia fillers. (b) An enlarged electron micrograph of the thinnest region of the rod-shaped specimen. The black region at the tip of the specimen was the tungsten deposited before the fabrication by FIB. Reprinted from Ref. [9], Copyright (2007) with permission from Elsevier.

$\alpha = 60^{\circ}$–70° in the conventional TEMT observations using planar sections.

It is of particular interest in material science as to how to accurately determine the structural parameters, e.g., volume

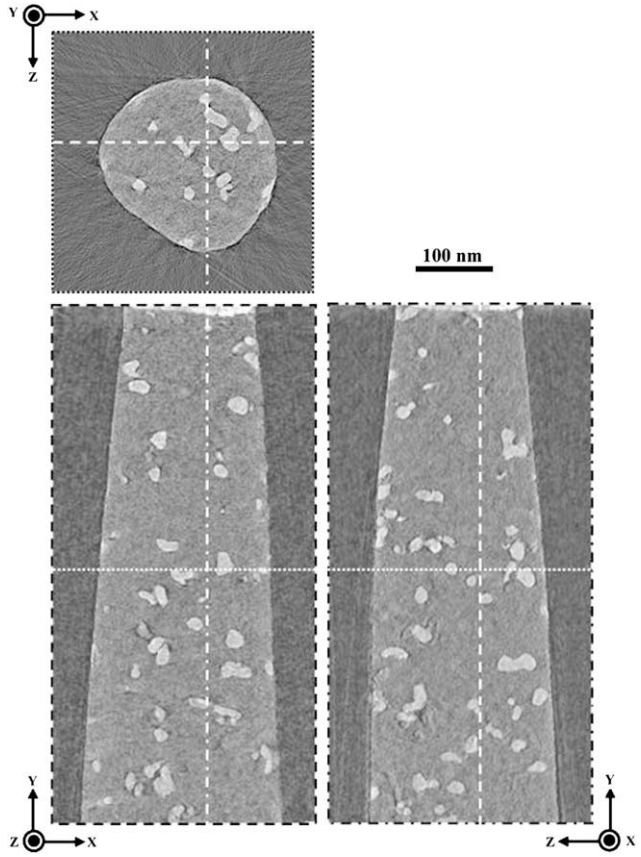

Fig. 7. Orthogonal views of 3D reconstruction of zirconia/polymer nanocomposite. The lines in each cross-section represent the positions of the other two orthogonal cross-sections (dotted line, *X*–*Z* plane; dashed line, *X*–*Y* plane; dot-dashed line, *Y*–*Z* plane). Reprinted from Ref. [9], Copyright (2007) with permission from Elsevier.

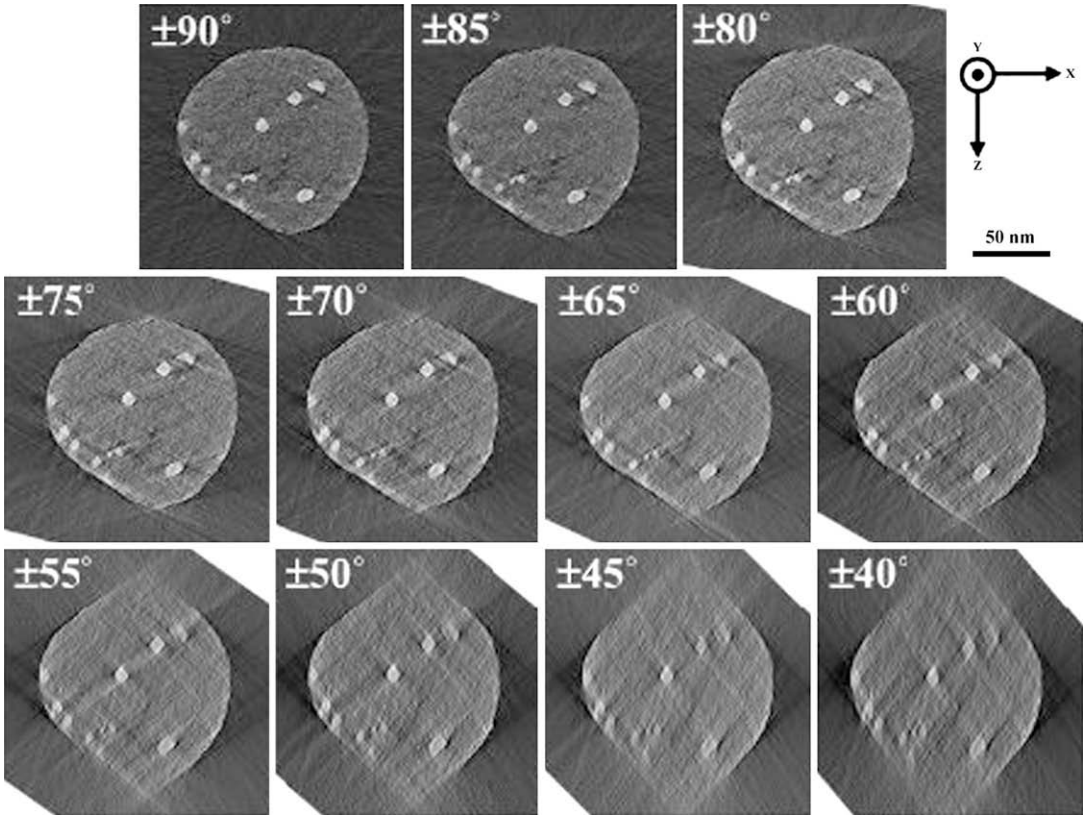

Fig. 8. A series of *X–Z* cross-sections of the same region in the rod-shaped specimen reconstructed at various maximum tilt angles, α, from 40° to 90° in 5° increments.

fraction, ϕ, of the zirconia grain. ϕ was measured as a function of α and is displayed in Fig. 9(a). The error bar in each measurement was associated with some uncertainties of the threshold in the binarization. ϕ decreased as α increased and approached a certain asymptotic value for a high α ($\alpha > 80°$). The known composition of the zirconia grain was 0.055 ± 0.005 from the preparation of the sample (dotted line), which is in excellent agreement with the measured asymptotic value, i.e., 0.055. The elongation of the zirconia grains and low signal-to-noise (S/N) ratio of the tomograms may be the cause of some deviation from the true value at small α values, which made the binarization of the tomogram somewhat difficult. It is worthwhile to note that we observed a 27% error in ϕ for the conventional TEMT, i.e., $\alpha = 60°$, in our zirconia/polymer nanocomposite. Furthermore, we recognized that the angular range of $\alpha \sim 70°$ may be required in order to attain a 10% error in ϕ in the nanocomposite.

4. Applications of TEMT to polymeric systems

TEMT is an ideal tool to characterize nano-structures and, as such, it has proven useful for providing high-resolution 3D information on a variety of polymeric structures, e.g., block copolymer nanoscale microphase-separated structures [8,41–44,34], clay/polymer nanocomposite materials [45], carbon black/natural rubber composites [46], etc. Some of these studies provided not only 3D pictures, but also a *quantitative* structural analysis. For example, in Section 4.3, the packing frustration of polymer chains in the block copolymer nano-structures will be discussed [42]. In the following sections, we will describe three applications of TEMT to polymer-related materials in order to demonstrate its potential utility in nanometer scale morphological characterizations.

4.1. A nanocomposite consisting of nano-fillers in a rubbery matrix: element-specific TEMT

As the first example, we deal with nanocomposites consisting of particulate nano-fillers in a polymer matrix. The nanocomposites have attracted substantial interest from researchers because they often exhibit unexpected properties synergistically derived from the two or more components. Composite systems based on organic polymers and inorganic clay minerals have been extensively studied due to their mechanical properties [47,48], gas barrier

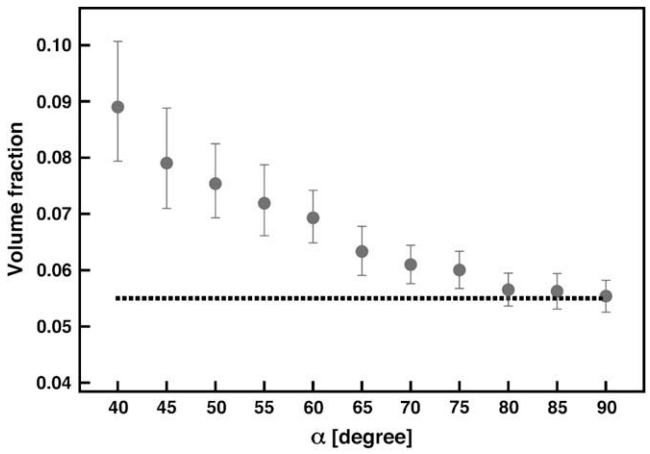

Fig. 9. Plot of volume fractions (zirconia/nanocomposite), ϕ, experimentally determined from the 3D reconstruction series from $\alpha = 40°$ to $\alpha = 90°$. Dashed line represents the known composition of the zirconia grain. The error bar on each point is associated with some uncertainty in the binarization process.

properties, etc. Nanometer size particulate fillers, e.g., carbon black (CB), silica (Si) nano-particles, etc., also form hybrids with organic polymers. They show a significant increase in both their static and dynamic moduli [49], strength [50], thermal and electrical conductivities [51–54]. Therefore, it is important to understand the structure–property relationship in order to achieve better properties in the nanocomposites. TEMT offers a detailed 3D characterization of the nanocomposites through various new structural parameters, some of which would never be obtained from other experimental techniques [45,46,55].

Among the various types of nanocomposites, as a representative example, the 3D direct observation and characterization of a nanocomposite with two kinds of particulate fillers in a rubbery matrix [46] will be presented here. One typical example is a composite of CB and Si nano-particles in a rubbery matrix. Hereafter, we call the nanocomposite CB&Si/NRBR [the matrix is a blend of natural rubber (NR) and polybutadiene (BR)]. In this composite, the CB increases the strength of the elastomer [56,57] and thus acts as a reinforcing filler, while the Si nano-particles may add tear strength, abrasion resistance and a reduction in the heat built-up. In order to improve and maximize such functionalities, it is first necessary to *independently* visualize the two kinds of fillers in the matrix and to determine their 3D spatial distributions.

Until recently, the filled polymers have been observed by TEM and other experimental techniques, e.g., scattering methods [58]. There are, however, several experimental difficulties for an accurate structural analysis; it is often difficult to distinguish the CB from the Si nano-particles under TEM in spite of their relatively large electron-density difference. For this problem, electron energy loss spectroscopy (EELS) [59], which enables us to obtain an elemental-mapped image, would be useful. Note that the EELS can be used together with the TEMT "TEMT–EELS" that will provide an elemental-mapped 3D image of materials. Detailed information about the nanocomposite and experimental protocols, especially about TEMT–EELS, can be found elsewhere [46].

Fig. 10(a) and (b) shows the digital slices of the TEMT and TEMT–EELS volume data at the same position of the CB&Si/NRBR specimen. A corresponding TEM micrograph is shown in Fig. 10(c). From the TEM micrograph, it is possible to judge the extent of the dispersion of the fillers in the rubbery matrix. However, because the fillers overlapped along the depth direction of the specimen (*Z*-direction) and resolution along this direction is lost in the TEM, the identification of respective fillers was impossible. In contrast, the digital slice of the 3D reconstruction [Fig. 10(a)] had a higher contrast than the TEM and the detailed features, i.e., the spatial arrangements of the fillers, were clearly observable. What is intriguing is that there are two kinds of fillers appeared differently in Fig. 10(a): One appeared solid, while the other was rather transparent in the middle with their edges having a strong contrast, somewhat like hollow spheres. Assignment of these two kinds of particles either to the CB or to the silica particle is necessary in order to understand the 3D morphology of the CB&Si/NRBR system.

In the TEMT–EELS experiments, a 3D reconstruction was carried out from the series of energy-filtered Si-mapped projections. Thus, the black particles in Fig. 10(b) correspond to the Si nano-particles. The image quality of the digital slice in the TEMT picture [Fig. 10(a)] is better than that in the TEMT–EELS [Fig. 10(b)] mainly due to the lower signal-to-noise ratio (*S*/*N*) of the Si-mapped projections and also due to the larger angular increment in the data acquisition of the TEMT–EELS experiment. Nevertheless, the position of the Si nano-particles was clearly seen.

Comparing Fig. 10(a) and (b), it was found that the aggregates of fillers marked by a circle were silica aggregates. Close examination of the two digital slices provides the following important result: Among the two kinds of fillers observed in Fig. 10(a), the hollow and solid particles are, respectively, the CB and Si nano-particles. This experimental finding is particularly important because it demonstrates that the two kinds of fillers can be *directly* distinguished by TEMT.

Based on the results found in Fig. 10, the arrangement of these two kinds of fillers can be directly visualized in 3D [see Fig. 11(a) below]. It was found that the aggregates consisted of only one species of the nano-particles. Namely, the CB and Si aggregates are made only of the CB and Si nano-particles, respectively. The size of each aggregate can be measured by separating the aggregates one from the other [46] using the particle analysis algorithm [45].

Although the 3D image shown in Fig. 11(a) exhibits by far richer structural information itself than the TEM micrograph, it only shows the outer shape of each aggregate. An algorithm based on the Monte Carlo method called a "particle-packing" algorithm was proposed to virtually pack as many spherical particles as possible inside the aggregates [46]. Fig. 11(b) shows the 3D images after applying the particle-packing analysis to the original TEMT–EELS image shown in part (a). The virtual CB and Si nano-particles did not fully occupy the corresponding regions, and hence the particle-packing algorithm is only semi-quantitative. Considering the fact that the CB and Si nano-particles are neither perfect spheres nor monodispersed, we regarded that the agreement of the volume fraction before and after the particle-packing analysis was acceptable. Most importantly, the shape of the aggregates was well

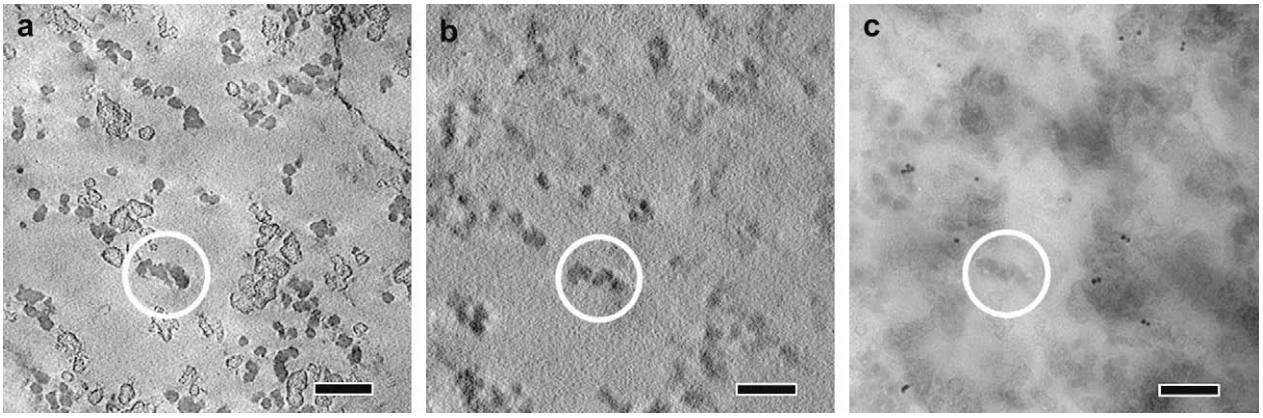

Fig. 10. (a) A digital slice of TEMT, (b) A digital slice image of 3D reconstruction from TEMT–EELS, and (c) TEM micrograph in the same field of view of the CB&Si/NRBR system. White circles indicate the same aggregate, i.e., Si aggregate, in the three pictures. Bar shows 100 nm. Reproduced with permission from Ref. [46]. Copyright 2007 American Chemical Society.

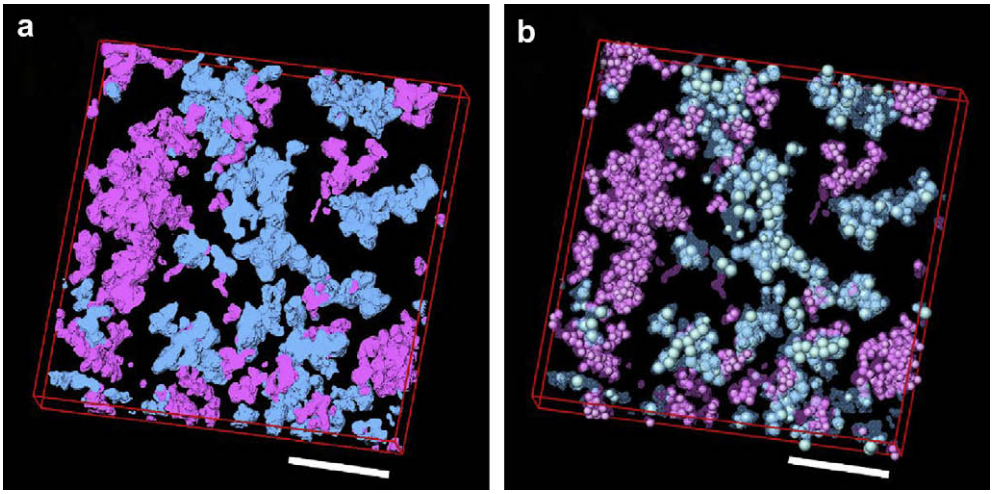

Fig. 11. (a) 3D reconstruction of CB&Si/NRBR system. Blue and red regions consist of CB and Si nano-particles, respectively. (b) 3D reconstruction of CB&Si/NRBR system after the particle-packing analysis. The blue and red balls represent the CB and Si nano-particles whose diameters are 22 and 17 nm, respectively. The CB and Si regions are translucent in part (b). Bar shows 200 nm. Reproduced with permission from Ref. [46]. Copyright 2007 American Chemical Society.

preserved even after the particle-packing analysis, and thus the analysis provides an intuitive understanding of the distribution of the primary nano-particles.

Such spatial position of each primary particle, i.e., individual CB and Si nano-particles, should be quite useful for correlating the internal morphology with various properties, e.g., the mechanical and electrical properties. For example, knowledge of the spatial arrangement of the nano-particles in the composite can be used to estimate the mechanical properties on the basis of a finite element analysis (FEA) [61,62], which would be a more accurate model than the conventional one in which the nano-particles have been *virtually* and *manually* arranged based on the insufficient 2D TEM images. Moreover, the persistent length of each aggregate, an important measure for understanding the electric conductivity of the nanocomposite materials, will be evaluated by examining the connectivity of the primary nano-particles [63].

4.2. A clay/polymer nanocomposite

Besides the CB&Si/NRBR system described in the previous section, TEMT was also applied to a clay/polymer nanocomposite, an organophilic montmorillonite (MMT) dispersed in poly (ethylene-*co*-vinylacetate) (EVA). The clay minerals are plate-like nano-fillers in this case. It is well known that the improvement in such properties strongly depends on their dispersion and orientation of the clay layers inside the polymer matrix [64,65]. 3D morphology of a clay/polymer nanocomposite was studied by TEMT with particular emphasis on the shape and orientation of each clay layer [45].

Fig. 12 shows a typical TEM image of the MMT/EVA nanocomposite. Cockle-like dark objects in the micrograph correspond to the clay layers. The exact shape and thickness of them were difficult to estimate.

The TEM micrographs similar to that shown in Fig. 12 but taken at different tilt angles were used to reconstruct a 3D image on the basis of the WBP. Three orthogonal cross-sections of the 3D TEMT reconstruction are shown in Fig. 13. Let us note, that the WBP method was carried out on *X*–*Z* plane. The *X*–*Y* plane (“lateral plane”) provides an image from the same direction as the TEM micrograph does, but TEM micrograph is a projection of the whole thickness of the specimen (ca. 150 nm as it was estimated from the *X*–*Z* plane in Fig. 13(a) and indicated by the dashed lines), while the *X*–*Y* plane displayed in Fig. 13(a) is a digitally sliced image with thickness being 0.58 nm. It is essential to note that the precisely aligned tilt series gives clear cross-sections from which the thickness of the section can be measured quantitatively.

In comparison with the conventional TEM micrograph (as demonstrated in Fig. 12), the digital slice again offered higher contrast as well as much more detailed structural information. This contrast enhancement was obtained due to the significant reduction of the overlap of the structural objects along the depth direction of the ultra-thin section (*Z*-direction). Another reason of the higher contrast was a significant noise reduction in the WBP calculation due to averaging many projections from various tilt angles. The thickness of each clay layers was found to be rather

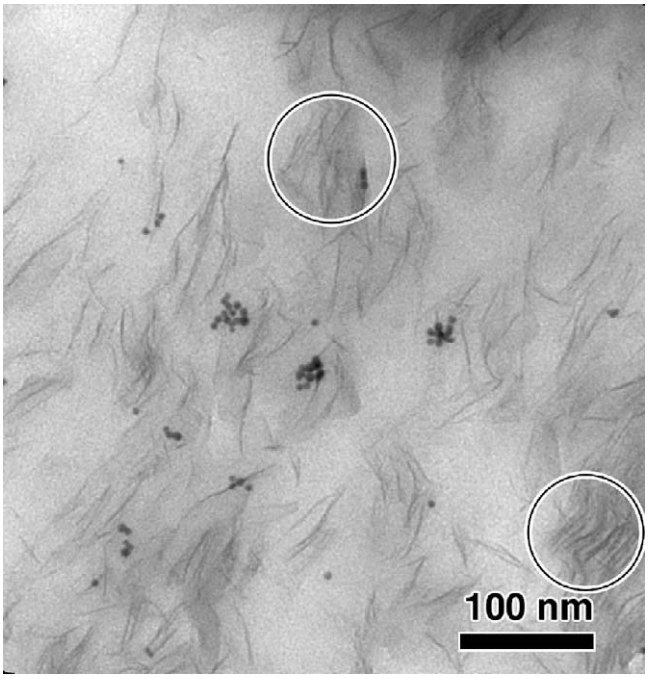

Fig. 12. TEM micrograph of clay/polymer nanocomposites. Thin dark lines are clay layers. The black dots in the TEM image represent the gold particles placed on the ultra-thin section. Reproduced with permission from Ref. [45]. Copyright 2006 Brill.

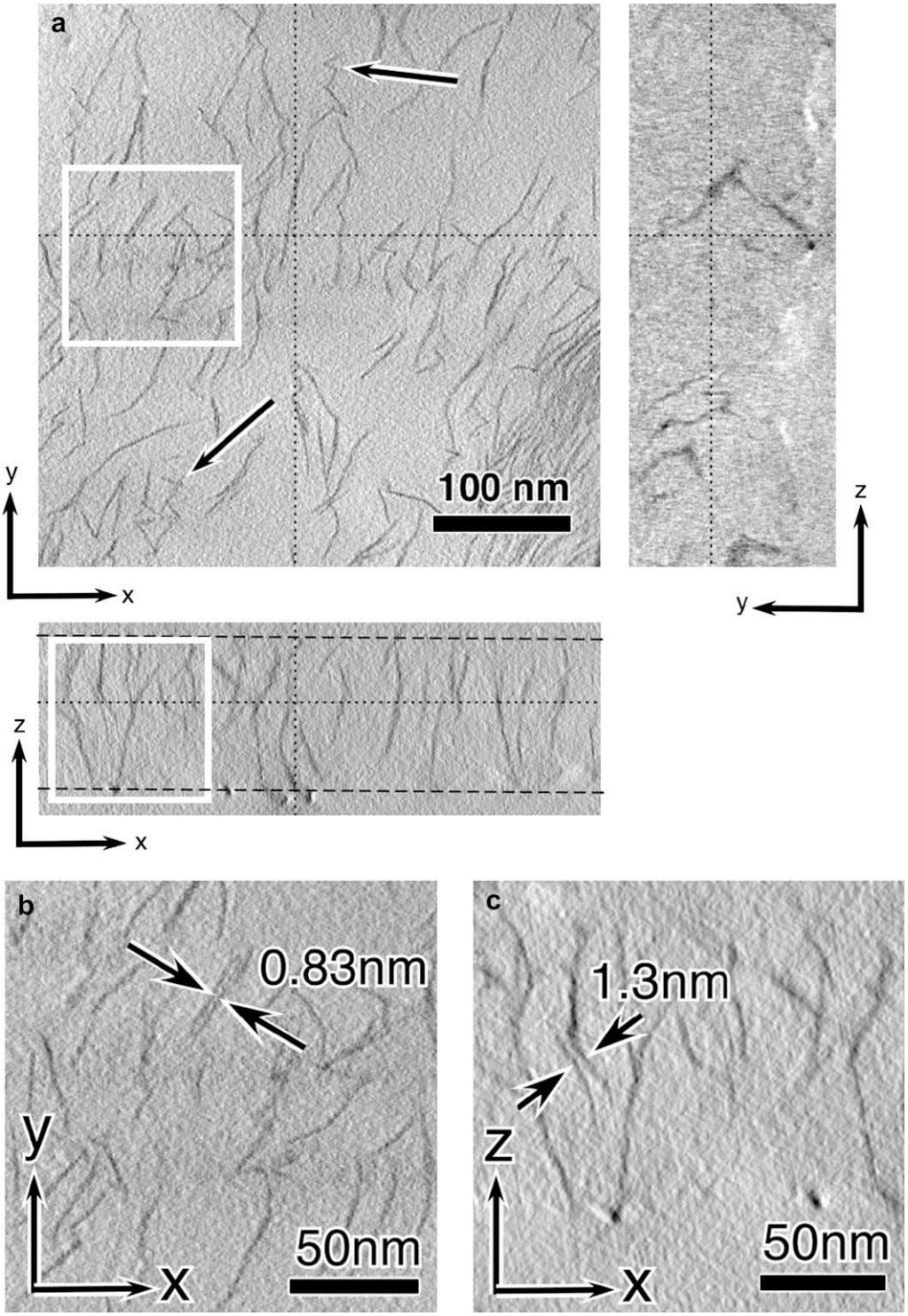

Fig. 13. (a) Orthogonal cross-sections of the 3D image of MMT/EVA nanocomposite obtained by TEMT. The *X*–*Y* cross-section provides an image from the same direction as the TEM micrograph (see Fig. 12). *Z*-direction is the direction along the sample thickness. The *X*–*Z* plane is the plane where the WBP method was carried out. (b) The enlarged *X*–*Y* cross-section of the white rectangle of (a). The shortest interlayer distance is 0.83 nm. (c) The enlarged *X*–*Z* cross-section of part (a). The shortest interlayer distance in this plane is 1.3 nm. Reproduced with permission from Ref. [45]. Copyright 2006 Brill.

uniform, ca. 1–2 nm, which is in a good agreement with the reported in the literature value [66]. It is interesting to note that some of the clay layers appeared to exhibit zigzag configuration (marked by arrows in Fig. 13(a)), which we call "card-house morphology". The MMT/EVA nanocomposite did not show any evidence of flow even at the temperature higher than the glass transition temperature of EVA. Since EVA matrix is not cross-linked, this phenomenon may be related to the card-house morphology in nanometer scale.

Fig. 13(b) and 13(c) displays enlarged views of *X*–*Y* and *X*–*Z* planes. The enlarged regions are indicated by white rectangles in Fig. 13(a). There are regions in the enlarged figures, where two clay

layers locate very close to each other. The shortest distance between the two adjacent layers defines the "line resolution" of the 3D reconstructed image. The line resolution in the *X*–*Y* and *X*–*Z* planes was 0.83 and 1.3 nm as indicated by arrows in Fig. 13(b) and (c), respectively. Such anisotropic spatial resolution of TEMT is due to the insufficient sampling of the TEM tilt series, i.e., the missing wedge problem as discussed above in Section 3.1.1 [36,37].

In order to find the interface between the clay and matrix polymer, the *X*–*Y* cross-sectional images were binarized by setting an appropriate threshold. The clay layers thus segmented were subjected for measurements of size, shape, orientation, etc. As a prelude to do such measurements, an algorithm called "3D particle analysis" was used to differentiate one clay layers to the other, the details of which are described elsewhere [45]. The anisotropic features of the clay layers, e.g., the aspect ratio and orientation, were determined by the ellipsoidal approximation [45]. The method includes the use of the inertia tensor, *I*, of an anisotropic particle. According to the theorem of tensors, *I* can be decomposed into a diagonal matrix:

$$I = P\begin{pmatrix} \lambda_1 & 0 & 0 \\ 0 & \lambda_2 & 0 \\ 0 & 0 & \lambda_3 \end{pmatrix} P^{-1}. \tag{4}$$

Here λ_1, λ_2 and $\lambda_3$are the eigenvalues of *I*. *P* is an invertible matrix consisting of the eigenvectors of corresponding eigenvalues. The following relation between the semi-axis length of the ellipsoid and the eigenvalues of the solid body holds [67]:

$$\lambda_1 = \frac{V}{5}\left(b^2 + c^2\right), \quad \lambda_2 = \frac{V}{5}\left(a^2 + c^2\right), \quad \lambda_3 = \frac{V}{5}\left(a^2 + b^2\right), \tag{5}$$

where *a*, *b* and *c* are the semi-axis length of the ellipsoid and *V* is the volume of the object. $V = (4\pi/3)abc$. Thus, the diagonalization of inertia tensor provides the aspect ratio of the anisotropic particle (clay layers in our case), and the eigenvectors provide the orientation of the particle.

Fig. 14(a) schematically displays such ellipsoidal approximation. We define the longest, intermediate, and shortest semi-axes of ellipsoid as *a*-, *b*- and *c*-axis, respectively. Fig. 14(b) shows the anisotropy of the clay layers: Each bar represents different clay layers and the height of the bar shows total length of three semi-axes of the corresponding ellipsoid. Each bar consists of three semi-axes in the order of the shortest to the longest axes from bottom to top. Each clay layer was numbered in the order of the volume. Up to clay number 70, the *c*-axis stayed rather constant around 2 nm while the other two axes dramatically increased, indicating that these clay layers exhibited more flattened shape. The *c*-axis should be closely related to the thickness of the clay layer in such a way that the twice of the *c*-axis approximately corresponds to the average thickness of the clay layer. Thus, from the ellipsoidal approximation, the average thickness of clay layer would be 4–5 nm, being contradict to the observed thickness, i.e., 1–2 nm (see Fig. 12). This is probably due to the fact that the clay layer is not flat but rather bent sheets. In some clays whose clay number is larger than 70, even the *c*-axis became larger than 2 nm. They may be either aggregate of multiple clay layers.

The orientation of the clay layers is another structural parameter that may be related to the mechanical and transport (gas barrier)

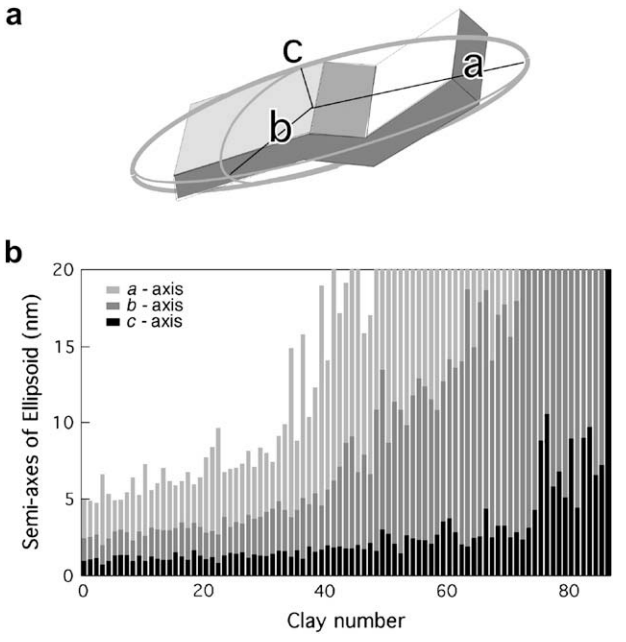

Fig. 14. (a) Schematic illustration of the ellipsoidal approximation of a clay layer. (b) Three semi-axes of 87 clay layers after the ellipsoidal approximation. The clay layers are labeled according to their volume: The volume increases with the clay number. Each bar shows three semi-axes of the corresponding ellipsoid in the order of the shortest to longest axes from the bottom to top. Reproduced with permission from Ref. [45]. Copyright 2006 Brill.

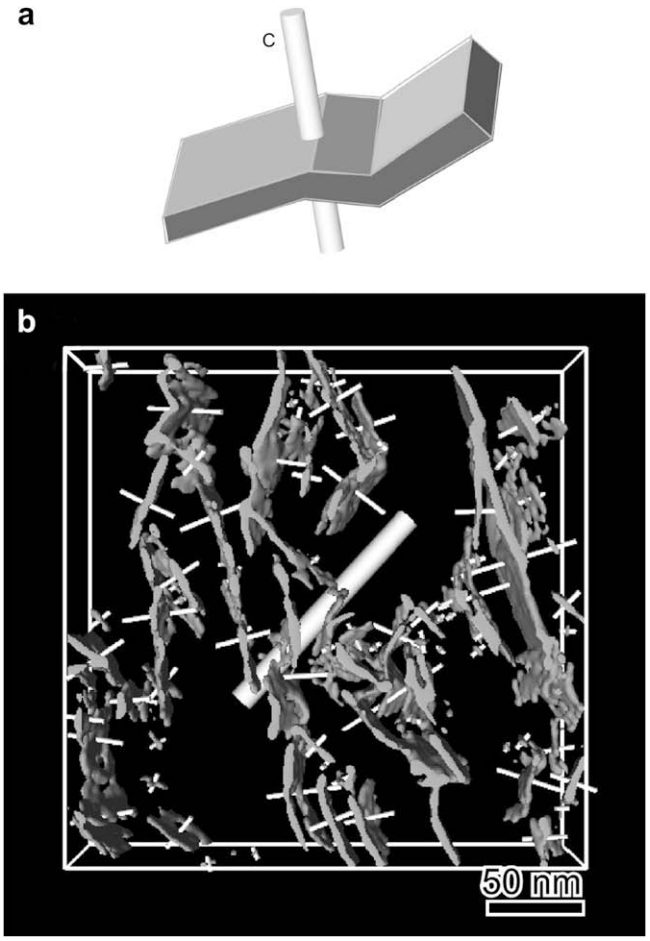

Fig. 15. (a) Schematic illustration of the normal vector of a clay layer. The direction of the normal vector is same as that of *c*-axis shown in Fig. 14(a). The length of the normal vector is proportional to the volume of the clay layer. (b) The normal vectors of the clay layers obtained from 3D particle analysis and ellipsoidal approximation are displayed as arrows. Reproduced with permission from Ref. [45]. Copyright 2006 Brill.

properties of the nanocomposite materials. In the 3D particle analysis and the ellipsoidal approximation, three normal vectors, i.e., eigenvectors, to the clay surfaces were estimated. As schematically shown in Fig. 15(a), the normal along the *c*-axis was chosen to be the representative normals of each clay layer. In Fig. 15(b), the normal vectors of clay layer were displayed as white arrows that skewer the clay layers. The length of the arrows is proportional to the volume of each clay layer. It seems that the orientation of the clay layers characterized by the arrows was rather random and did not show any specific direction. Thus, a volume-averaged normal of the clay/polymer nanocomposite was estimated and displayed as a thick cylinder in Fig. 15(b). The various structural parameters obtained in the present section will open the way to the comprehensive understanding of a variety of physical properties of the nanocomposites.

4.3. Microphase-separated morphologies in block copolymers

Following the classical work done by Spontak et al. [8], there are a couple of morphological studies in the 1990s [68,41,69]. The number of studies using TEMT on block copolymers is increasing rapidly, especially in the past couple of years. The technique has been mainly used for structural investigations using its 3D visualization capability [70,43,44,71–79]. In some cases, however, some geometrical analyses of the microphase-separated structures have been carried out in order to understand their stability [42] and topological features [80]. In the following sections, we show three examples in which TEMT played essential roles to provide new insights into physics behind the self-assembling processes and structures.

Block copolymers exhibit periodic nano-structures due to immiscibility between the dissimilar (A and B) sequences [3,81]. Classical block copolymer nano-structures include spheres of A(B) on a body-centered cubic lattice in a B(A) matrix, cylinders of A(B) on a hexagonal lattice in a B(A) matrix, and co-alternating lamellae. Of considerable recent interests are several complex (bicontinuous) nano-structures – the perforated lamellar (PL), gyroid (G) and double-diamond (D) morphologies [82–87]. These nano-structures may develop if the copolymer composition, *f*, falls within a narrow range between the cylindrical and lamellar morphologies.

Fig. 16 shows an example of the G morphology observed by TEM. The characteristic "wagon wheel" projection was observed in the figure. The block copolymer nano-structures presented in Fig. 16 once believed to be D [82], exemplified by a Schwarz D surface with $Pn\bar{3}m$ symmetry, have been reclassified [88] on the basis of the small angle X-ray scattering (SAXS) signatures as G, which is represented by the Schoen G surface with $Ia\bar{3}d$ symmetry. Identification of complex nano-structures by TEM is often inconclusive, because they appear identical along several projection axes.

Complex nano-structures similar to the above block copolymer morphology also develop in surfactant and lipid systems due to the formation of surfaces with constant mean curvature (CMC) that minimizes contact between immiscible moieties [89]. Because block copolymer microphase-separated structures share common topological features with those of other self-organized systems, the concept of CMC minimal surfaces has been used [83] to explain the stability of complex block copolymer microphase-separated structures. On the basis of the self-consistent field theory (SCFT), Matsen and Bates [90,91] have proposed that the area-averaged mean curvature, $\langle H \rangle$, governs the gross morphology (lamellar, bicontinuous, cylindrical or spherical), whereas the standard deviation of the mean curvature distribution, σ_H, determines the delicate stability of the complex microphase-separated structures (G, D or PL). This additional consideration results from "packing frustration" [92] implies that, while a surface strives toward CMC, the mean curvature cannot be constant everywhere along the interface because the microdomain-forming blocks must uniformly fill space in the most entropically favored manner. Thus far, neither $\langle H \rangle$ nor σ_H has been measured experimentally despite their apparent importance.

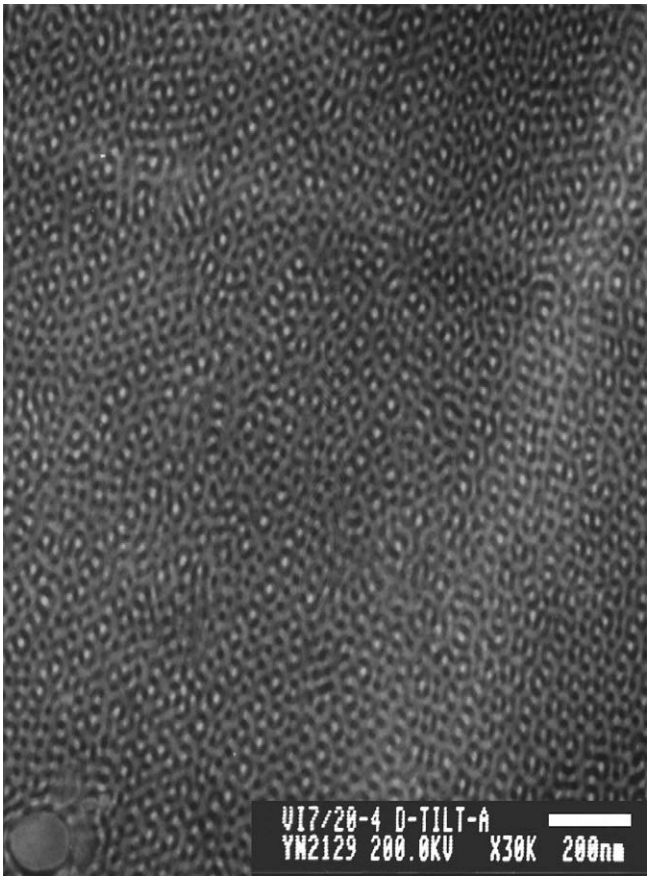

Fig. 16. TEM micrograph of poly(isoprene-*block*-vinylpyridine) diblock copolymer. Due to O_sO_4 staining, isoprene-rich regions are electron-opaque and appear dark. The "wagon wheel" projection associated with the [1 1 1] axis of G morphology is observed.

4.3.1. Bicontinuous block copolymer morphology

A poly(styrene-*block*-isoprene-*block*-styrene) (SIS) triblock copolymer was synthesized by living anionic polymerization. Details of the experimental protocols and TEMT measurements are provided elsewhere [68,93,94].

Fig. 17(a) shows the reconstructed 3D image of the microphase-separated structure in the SIS triblock copolymer. Volumetric analysis of the reconstruction yields the styrene volume fraction $f_S = 0.33$, in excellent agreement with the known composition of the copolymer [$f_S = 0.32$]. The light and dark channel networks evident in Fig. 17(a) both represent the S microphase. They are shaded differently to demonstrate that the two S channel networks do not intersect. For the sake of clarity in this figure, the I microphase is transparent. A crystallographic analysis of Fig. 17(a) identifies that the microphase-separated structure is G.

Displayed in Fig. 17(b) is a model bicontinuous morphology generated from the Schoen G surface. The trigonometric approximation used to generate this surface is given by

$$g(x,y,z) = \cos\frac{2\pi x}{L}\sin\frac{2\pi y}{L} + \cos\frac{2\pi y}{L}\sin\frac{2\pi z}{L} + \cos\frac{2\pi z}{L}\sin\frac{2\pi x}{L}. \quad (6)$$

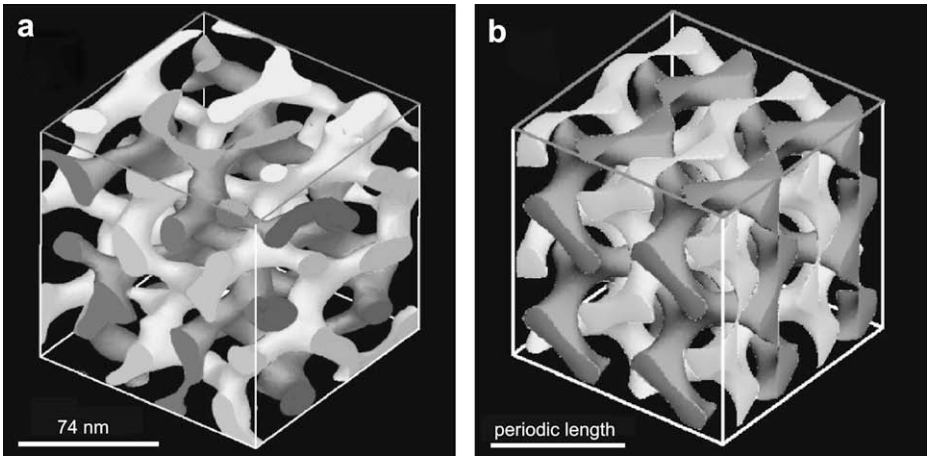

Fig. 17. Transmission electron microtomograph of the gyroid morphology in an SIS triblock copolymer (a), and the CT model based on Schoen's gyroid surface (b). The non-intersecting light and dark channels correspond to the minority microphase (S in the SIS copolymer), while the majority (I) microphase is transparent. The edge of each cube equals twice the periodic length, and the top cross-section identifies the (001) plane. The lattice constants of this nano-structure are $a = 78$ nm, $b = 71$ nm, $c = 74$ nm. Reprinted figure with permission from Ref. [42]. Copyright 2000 by the American Physical Society.

Here L denotes the crystallographic unit cell edge of the gyroid. The periodic minimal surface, which divides space equally, is obtained by setting $g(x, y, z)$ equal to zero. To emulate the microphase-separated nano-structure of the SIS copolymer with $f_S = 0.33$, a new model interface is formed by translating the interface obtained from Eq. (6) along its normals by an equal distance everywhere. Two parallel surfaces with opposite direction but the same displacement, selected so that the volume fraction of the swollen microphase is equal to 0.67, are consequently generated [95]. The resultant morphology constitutes an approximate model of the hypothetical CMC interface and, following Hajduk et al., [85] serves as the constant-thickness model. Interfacial curvature distributions were evaluated from the 3D morphologies in Fig. 17 according to an algorithm previously developed [95].

Fig. 18 shows a surface contour representation of the joint probability density, $P(H, K)$, measured from the G morphology. Included in this figure are the marginal probability densities of the mean and Gaussian curvatures – $P_H(H)$ and $P_K(K)$, respectively [95,42]. According to Fig. 18, most of the interface (77%) possesses $K < 0$, indicating that (i) the two principal curvatures (κ_1 and κ_2) have opposite signs and (ii) most of the interface is hyperbolic. A qualitative conclusion that can be drawn from Fig. 18 is that, because H is not constant everywhere along the interface, the CMC representation *does* not accurately represent the G morphology.

The interfacial curvature probability densities are displayed in Fig. 19(a) and (b) for the G morphology in the SIS copolymer and the constant-thickness model surface, respectively. To facilitate comparison, $P_H(H)$, $P_K(K)$ and $P(H, K)$ have been scaled with respect to the interfacial area per unit volume, Σ, in the following way:

$$\tilde{P}_H\left(\tilde{H};t\right) = \Sigma(t)P_H(H;t), \tilde{P}_K\left(\tilde{K};t\right) = \Sigma(t)^2 P_K(K;t), \tag{7}$$

and

$$\tilde{P}\left(\tilde{H},\tilde{K}\right) = P(H,K)\Sigma^3. \tag{8}$$

Here, $\tilde{H} = H\Sigma^{-1}$ and $\tilde{K} = K\Sigma^{-2}$, with $\Sigma = 0.070$ and $0.074\ \mathrm{nm}^{-1}$ for the SIS copolymer and constant-thickness model, respectively. Close examination of the scaled probability densities in Fig. 19(a) reveals that a part of $\tilde{P}(\tilde{H},\tilde{K})$ for the SIS G morphology possesses $\tilde{H} < 0$ and $\tilde{K} > 0$, implying that the interface is an elliptic surface curved inward relative to the I microphase. Such interfacial concavity is not evident from $\tilde{P}(\tilde{H},\tilde{K})$ derived from the constant-thickness model of the G morphology in Fig. 19(b), in which nearly all of the measured points possess $\tilde{K} < 0$. In this sense, the so-called G morphology in the SIS copolymer differs markedly from the mathematical G surface.

On the basis that interfacial tension constitutes the dominating factor for structure formation in microphase-separated block copolymers, Thomas et al. [83] have proposed that the complex microphase-separated structures formed in block copolymers correspond to area-minimizing surfaces. From the extensive SCFT calculations, Matsen and Bates [90,91] found that an equally important, but thus far disregarded, factor in block copolymer nano-structure stability is the packing frustration [92]. For the

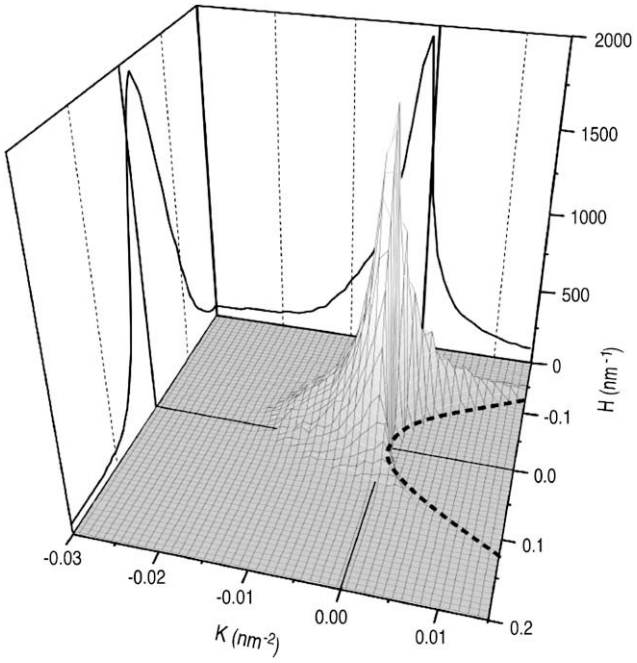

Fig. 18. Surface contour representation of the joint probability density, $P(H, K)$, measured from the G morphology of the SIS triblock copolymer. Marginal probability densities, $P_H(H)$ and $P_K(K)$, are also shown. The dashed parabolic curve represents $K = H^2$. The curvature is arbitrarily chosen to be positive if the center of the osculating circle resides within the PI microphase. Reprinted figure with permission from Ref. [42]. Copyright 2000 by the American Physical Society.

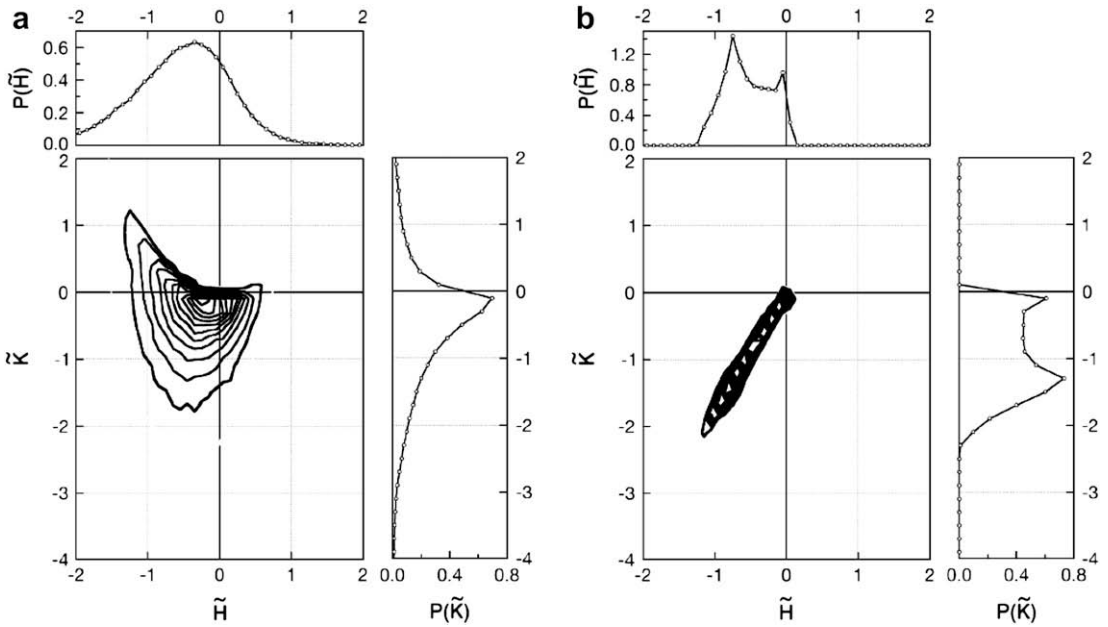

Fig. 19. Contour map of the scaled joint probability density, $\tilde{P}(\tilde{H},\tilde{K})$, and its marginal probability densities, $\tilde{P}_H(\tilde{H})$ and $\tilde{P}_K(\tilde{K})$, for (a) the G morphology of the SIS triblock copolymer and (b) the constant-thickness model of the G surface [Eq. (6)]. Reprinted figure with permission from Ref. [42]. Copyright 2000 by the American Physical Society.

minority blocks of an ordered copolymer to fill space uniformly, the interface self-adjusts so that no blocks are excessively stretched. This entropic consideration causes the interface to deviate from CMC (with $\sigma_H \approx 0$), in which case σ_H provides a measure of packing frustration and nanostructural stability. Although predicted $\langle H\rangle$ and σ_H are only available for diblock copolymers [91] (which differ from the present triblock copolymer in molecular architecture), it is worthwhile to compare the experimental interfacial curvature data obtained here with SCFT predictions.

The unperturbed statistical end-to-end distance of the SIS triblock copolymer, R_0, of our SIS triblock copolymer is estimated to be $R_0 \simeq 22$ nm [42]. The probability density measured for the G morphology in the SIS copolymer yields $\langle H\rangle = 0.034\ \text{nm}^{-1}$ and $\sigma_H = 0.042\ \text{nm}^{-1}$, which can likewise be expressed as $\langle H\rangle = 0.74R_0^{-1}$ and $\sigma_H = 0.91R_0^{-1}$. Assuming that the unperturbed chain length R_0 remains constant, we find that $\langle H\rangle$ and σ_H from the constant-thickness model of the G morphology are $0.92R_0^{-1}$ and $0.55R_0^{-1}$, respectively. According to SCFT predictions [91] for an AB diblock copolymer with $f_A = 0.34$, $\langle H\rangle = 0.70R_0^{-1}$ and $\sigma_H = 0.12R_0^{-1}$ at $\chi N = 20$. Here, χN is a measure of the copolymer segregation power, wherein χ represents the Flory–Huggins interaction parameter. χN for our SIS triblock copolymer is about 64. Thus, the value of $\langle H\rangle$ derived from the probability densities in Fig. 19(a) for the G morphology in the SIS triblock is in reasonably good agreement with that predicted by SCFT, whereas the value of σ_H obtained here is higher than what is predicted. This discrepancy may reflect noise inherent in the TEMT reconstruction or, alternatively, the large difference in χN (Matsen and Bates [91] predict that σ_H should increase with increasing χN). Further analysis of the factors influencing σ_H is needed for more accurate comparison between experiment and theory.

4.3.2. Grain boundary morphologies

Here in this section, let us describe another example in which TEMT plays a critical role in studying an "old" bur somewhat "unsolved" subject in block copolymer morphological studies.

The morphology of boundary regions between grains influences the mechanical, electrical, and diffusional properties [96,97] of a block copolymer to a great extent [98–100]. The 3D continuity of each microdomain at the grain boundary is not trivial, especially in lamellar and cylindrical structures due to their high orientation and non-equilibrium nature. One of the grain boundary morphologies in lamellar morphology, the twist grain boundary (TGB), at which two lamellar nanodomains orthogonally intersect remains unsolved because a 2D periodic minimal surface, Scherk's first surface, was once hypothesized as a model of such grain boundary morphology but never experimentally ascertained. Fig. 20 shows a TEM micrograph of the SI diblock copolymer. As marked by an ellipsoid, a crosshatched region characteristic of the TGB was observed.

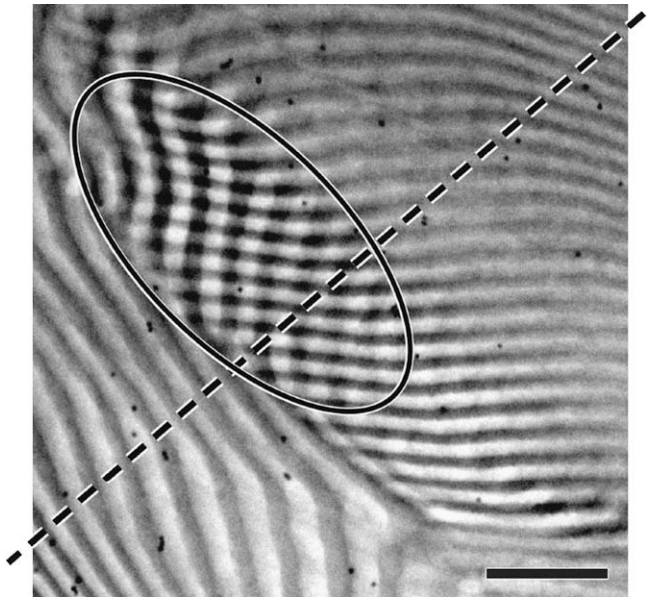

Fig. 20. TEM micrograph of SI diblock copolymer. Black and white domains correspond to PI and PS nanodomains, respectively. The dashed line represents an axis around which the region marked by the ellipsoid was tilted. Small dots are Au nano-particles (diameter: 5 nm). Bar indicates 200 nm. Reproduced with permission from Ref. [72]. Copyright 2006 American Chemical Society.

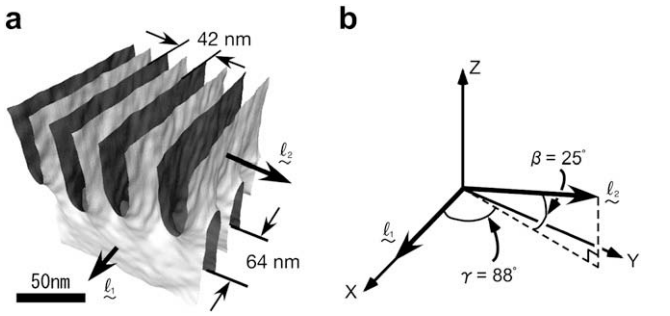

Fig. 21. (a) Surface-rendered 3D image of grain boundary in SI diblock copolymer. The interface is colored gray on one side and white on the other. The nanodomain looking toward the gray side is the PI nanodomain, while the PS nanodomain is toward the white side. Lamellar normals of upper and lower grains are displayed by arrows. Tilt and twist angles between the two lamellar grains are demonstrated in (b), in which the normal of the lower lamella, ℓ_1, lies along the *X*-axis. Reproduced with permission from Ref. [72]. Copyright 2006 American Chemical Society.

Depicted in Fig. 21(a) is the 3D surface-rendered image, in which the TGB was clearly demonstrated. The upper and lower lamellar nanodomains almost perpendicularly intersect. The 3D Fourier transformation (FT) was separately carried out in the upper and lower lamellar domains to calculate the structure factors of the domains. The "diffraction spots" of the structure factors were used to determine the lamellar normals, which are schematically shown by ℓ_1 and ℓ_2 in Fig. 21. ℓ_2 is aligned with the *X*-axis. The twist angle, γ, was found to be 88°. The tilt angle, β, was 25°. Note that the ideal TGB has $\beta = 0°$. Thus, rigorously speaking, the grain boundary observed here was *not* a perfect TGB, but yet it may be within the TGB category, at least in an experimental sense.

Let us now compare the experimentally obtained TGB with Sherk's first surface. Parts (a) and (b) of Fig. 22 show the TGB obtained from the TEMT viewed from two different angles, while parts (c) and (d) are, respectively, the computer-generated Scherk's first surfaces using the following equation for Cartesian coordinates (x, y, z) [98] from similar directions as in Fig. 22(a) and (b).

$$\exp z \cos x = \cos y. \tag{9}$$

On the basis of these figures, the observed TGB appeared to be quite similar to Scherk's first surface [see especially Fig. 22(b) and (d)]. Besides such a qualitative comparison, the area-averaged curvatures of the interface between the PI and PS phases as well as the interfacial area per unit volume were actually measured, from which the experimentally obtained grain boundary morphology had the characteristics of a saddle-like hyperbolic surface and was found to be quite similar to Scherk's first surface [72].

4.3.3. 3D morphology during order–order transition in a block copolymer

The self-assembling process, e.g., the order–order transitions (OOTs), is also a suitable theme for TEMT because the boundary morphologies between the two existing structures, by which the mechanisms of the OOTs are inferred, are often complicated in 3D.

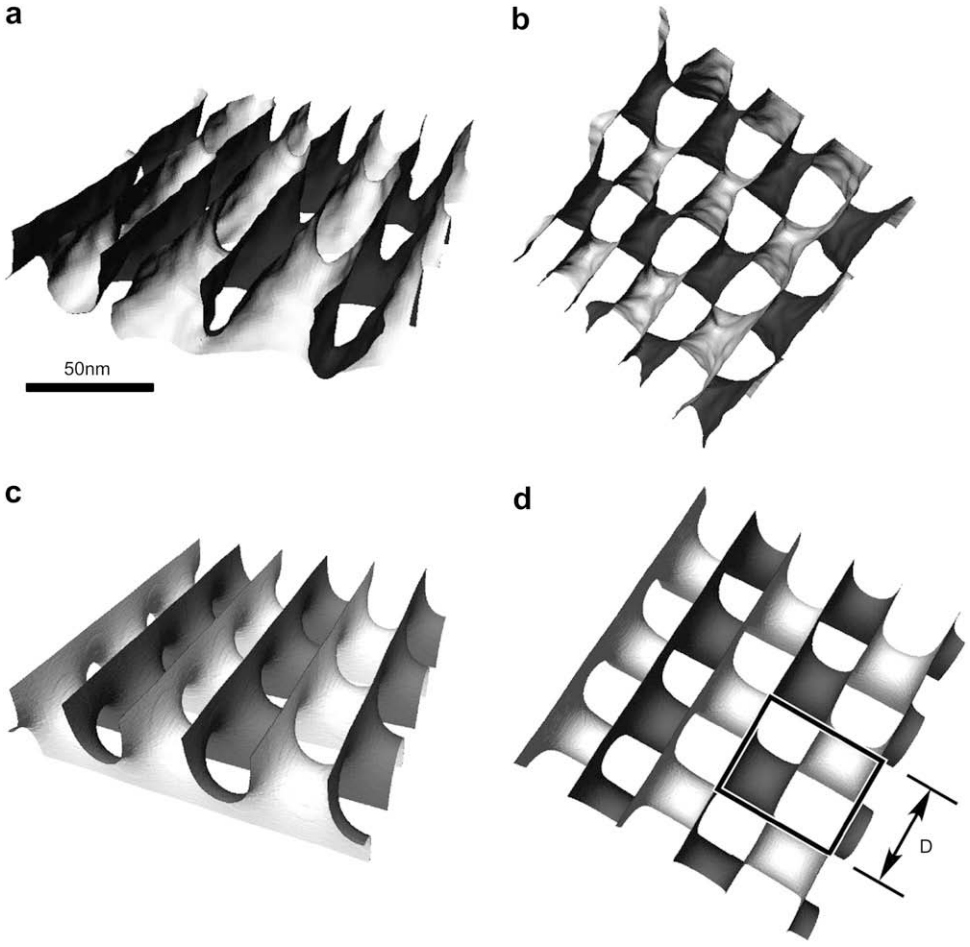

Fig. 22. Experimentally observed grain boundary of SI diblock copolymer viewed from (a) side and (b) top. Corresponding Scherk's first surfaces are shown in (c) and (d). In (d), unit cell viewing from the top is shown by the bold boxed region. Reproduced with permission from Ref. [72]. Copyright 2006 American Chemical Society.

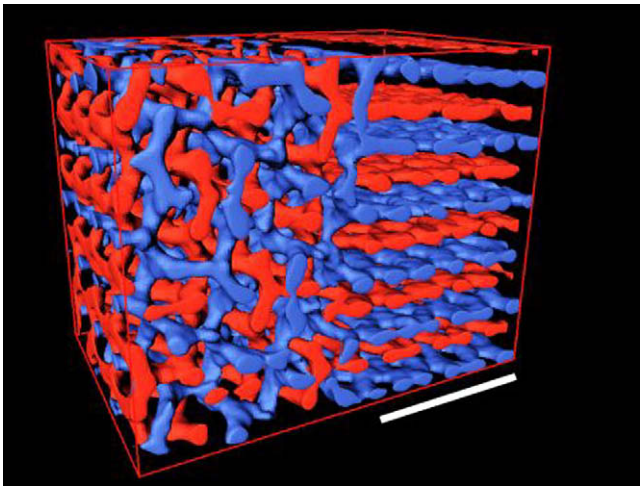

Fig. 23. 3D morphology of poly(styrene-*block*-isoprene) (SI) block copolymer during the OOT from HPL (right) to G (left). The gyroid structure has $Ia\bar{3}d$ symmetry. Blue and red microdomains consist of polystyrene and continuous through the boundary. Non-intersecting PS microdomains independently and are periodically connect to the PL layers. Scale bar is 100 nm. This is collaborative work with Prof. Taihyun Chang at Pohang University of Science and Technology, Korea.

The OOT between the PL and G has been first reported by Dohi et al. [101] followed by Mareau et al. [102], in which the connectivity of the two non-intersecting G microdomains to the PL layer was beautifully visualized [see Fig. 23] [103]. TEMT was also used to investigate the OOT between G and cylindrical structures [104]. In both OOTs, epitaxial growths of the newly forming microdomains were observed.

In addition, combination of TEMT and the SCFT calculation gives the block chain conformation inside the microdomains [105], which would hopefully yield basic understanding of block copolymer self-assembly from the molecular level.

5. A new structural analysis for a block copolymer thin film

5.1. Background

As described in Section 1, there are advantages and disadvantages in microscopy and scattering methods. In this section, we demonstrate a novel structural analysis that combines the real space (TEMT) and the reciprocal space (Neutron reflectivity, NR) methods for structural characterization of microphase-separated structures that remain intact today [106].

When the microphase-separated structures are confined in a thin film whose thickness is on the order of 10–100 nm, the surface interaction (between the block copolymer and substrate or between the block copolymer and air surface) as well as the confinement significantly affects the microphase-separated structures [107]. Due to such additional interesting effects on the self-assembling processes, the structure formation and morphologies in the block copolymer thin films have been extensively studied in academia [108]. They have likewise drawn considerable attention in many technological areas such as microelectronics [109–112] and nanoporous films [113,114]. Guarini et al. reported that block copolymer thin films can be used as the mask layers for dense nanoscale dot patterning [109]. Applications of block copolymer thin film morphologies to the high surface area substrates for capacitors and biochips, quantum dot arrays for nonvolatile memories, silicon pillar arrays for vertical transistors or field-emission displays may be possible [109].

NR is one of the most useful methods for investigating microphase-separated structures of block copolymer thin films [108]. It provides a concentration (density) profile of one of the components with the very high precision of 0.5 nm. Some important pieces of structural information about block copolymer thin films, e.g., the location of junctions between dissimilar sequences, chain ends inside the microdomains and the interfacial thickness, have been investigated using NR [115–118].

Although powerful, NR first requires a hypothesized concentration profile for data analysis. The concentration profile assumed along the *Z*-direction, i.e., the direction normal to the substrate, is used to fit the experimentally obtained NR profile [119]. This "fitting" protocol of the concentration profile to the NR profile heavily depends on the initial concentration model [120]. Therefore, until recently, NR has been more or less limited to rather simple morphologies that can be easily hypothesized, e.g., a lamellar morphology parallel to the substrate [115–118].

Although some applications seek to take advantage of the cylindrical microdomains in the block copolymer thin films, there are only a few studies dealing with cylinders [121,122] and, to the best of our knowledge, no studies dealing with other types of microphase-separated structures in the block copolymer thin films exist due to some difficulties in assuming the appropriate initial concentration profiles for these morphologies. Therefore, it is critical to establish a methodology to estimate the initial concentration profiles. In the section below, we would like to demonstrate a novel protocol that the combination of TEMT and NR would be capable of characterizing block copolymer thin films *regardless of the type of morphologies*.

5.2. Neutron reflectivity measurement

A poly(deuterated styrene-*block*-2-vinylpyridine) (dPS-*b*-P2VP) block copolymer that forms a cylindrical morphology in the bulk state was used [106]. The block copolymer was spun-coated on a Si substrate, which was extensively annealed (170 °C for 14 days) before the NR experiments. The measured NR profile from the dPS-*b*-P2VP, R_{exp}, is shown by the open circles in Fig. 24 where the reflectivity, R, is plotted versus the magnitude of the scattering vector along the *Z*-direction, q_z. A rather featureless NR profile was obtained from the thin film, indicating that the microphase-separated structure inside the thin film was not very ordered one.

The microphase-separated structure formed hexagonally packed cylindrical microdomains in the bulk and so this structure may be the first choice to start analyzing the NR profile as illustrated in Fig. 24(b): The cylinders are assumed to be aligned parallel to the substrate according to the results from previous studies [121,35,123]. The hypothetical model is based on the structural parameters determined from the bulk state and from the film thickness separately measured by AFM. The scattering length density profile along the direction perpendicular to the film surface was calculated from the model, b/v_{model}, which is shown by the dashed line in Fig. 24(c). Because b/v is smaller for P2VP than for dPS, the peak-top and peak-bottom correspond to the dPS and P2VP phases, respectively (b and v are the scattering length and the molar volume, respectively). There are five bottoms in Fig. 24(c), each of which corresponds to the layer of the P2VP cylinders. It is obvious that the calculated NR profile based on b/v_{model}, R_{model}, did not reproduce the NR profile over the entire range of q_z.

The algorithm proposed by Parratt based on a recursive calculation method [119,120] was employed to fit the R_{model} to R_{exp}. The resulting best-fit profile and the corresponding b/v are shown by the solid line in Fig. 24(a) and (c), respectively. Although the NR profile after the fitting approached R_{exp}, there was still a considerable deviation especially for the large q_z. This result again indicates that the microphase-separated morphology was not a simple one as hypothesized. Because the NR profile did not

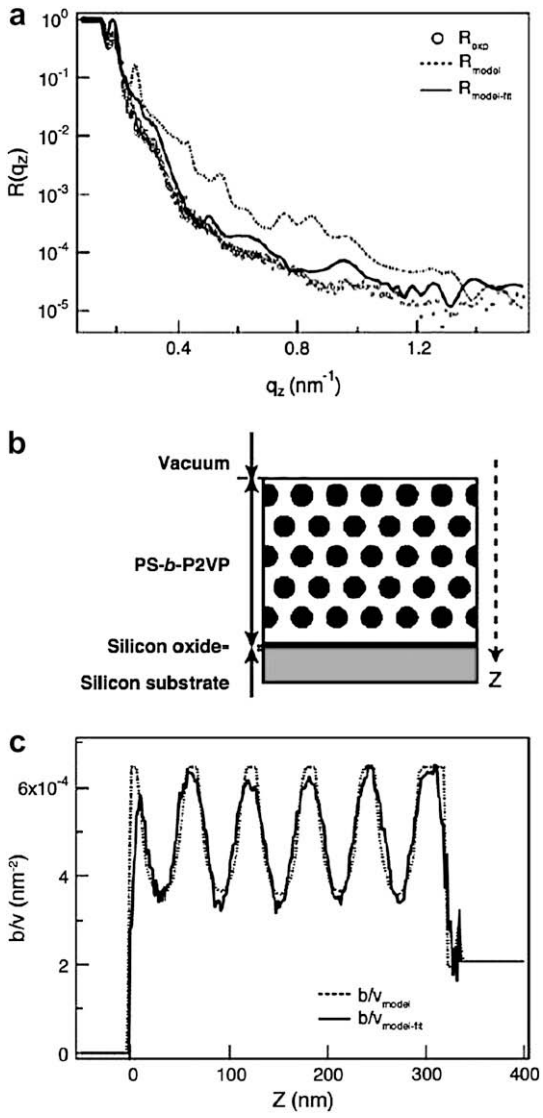

Fig. 24. (a) NR profile of the dPS-*b*-P2VP thin film (open circles). The dashed line is the calculated reflectivity profile based on the hypothetical model in which the hexagonally packed cylinders are aligned parallel to the substrate. The corresponding b/v is shown by the dashed line in part (c). The dashed line was used as an "initial guess" in the fitting protocol [119,120]. The solid line represents the best-fit NR profile after the fitting [the corresponding b/v is the solid line in part (c)]. (b) A cross-sectional view of the hypothesized initial model of the dPS-*b*-P2VP thin film cast on a Si substrate. Dark circles and white domain are the edge-on view of the P2VP cylinder and the dPS matrix, respectively. The *Z*-direction in normal to the film surface. (c) Scattering length density profile, b/v, of the dPS-*b*-P2VP. The dashed line is the calculated profile from the hypothesized model shown in part (b). The solid line is the calculated b/v profile from the best-fitted reflectivity profile.

show distinctive peaks, it is intrinsically difficult to have a precise and unique best-fit profile unless we have a realistic model for b/v as the initial guess.

5.3. A new method: combination of NR and TEMT

A cross-sectional section (specimen) for the TEMT experiment was prepared by the FIB method from exactly the same spun-cast sample used in the NR experiments. The reconstructed 3D images of the dPS-*b*-P2VP thin film are displayed in Fig. 25 from two different viewpoints, in which only the P2VP phase is shown (the dPS phase is transparent). *Z*-direction corresponds to the depth direction of the dPS-*b*-P2VP thin film. Although the majority of the cylindrical microdomains was oriented parallel to the substrate and formed six layers as indicated by arrows in Fig. 25, they did not form hexagonally packed cylinders as hypothesized in Fig. 24(b). In addition, the cylindrical microdomains aligning normal to the film surface that connected the adjacent layers are also found and indicated by the white circle in Fig. 25. It seemed that the cylindrical microdomains were interconnected through such vertical cylinders.

The scattering length density profile obtained from the TEMT image shown in Fig. 25, b/v_{TEMT}, is shown by the dashed line in Fig. 26(a). The NR profile based on this b/v_{TEMT} was obtained from the TEMT experiments, R_{TEMT}, and shown in Fig. 26(b). Comparing the previous results in Fig. 24(a) and (b), i.e., R_{model} and b/v_{model}, (i) R_{TEMT} exhibited a more accurate NR profile than the R_{model} did, and (ii) b/v_{TEMT} had six peaks (as b/v_{model} did), but their heights were distinctively different from those in the b/v_{model}, especially in the middle of the thin film ($100\ \mathrm{nm} \leq Z \leq 250\ \mathrm{nm}$). R_{TEMT} reproduced R_{exp} very well at a low q_z ($q_z < 0.4\ \mathrm{nm}^{-1}$), but not in the high q_z region, indicating that the b/v_{TEMT} (and thus TEMT) captures the global feature of the dPS-*b*-P2VP thin film morphology, but the structural details were lost.

The b/v_{TEMT} was subsequently used as the initial guess for the fitting. The resulting scattering density profile, $b/v_{\mathrm{TEMT\text{-}fit}}$, and the corresponding reflectivity profile, $R_{\mathrm{TEMT\text{-}fit}}$, after the fitting [119] are denoted by the solid lines in Fig. 26(a) and (b), respectively. $R_{\mathrm{TEMT\text{-}fit}}$ showed excellent agreement with R_{exp}, much better than R_{model} did.

The volume fractions of the dPS and P2VP blocks normal to the substrate ($\phi_{\mathrm{dPS\text{-}TEMT\text{-}fit}}$ and $\phi_{\mathrm{P2VP\text{-}TEMT\text{-}fit}}$) were calculated from the scattering density profile obtain from the fitting, $b/v_{\mathrm{TEMT\text{-}fit}}$, in

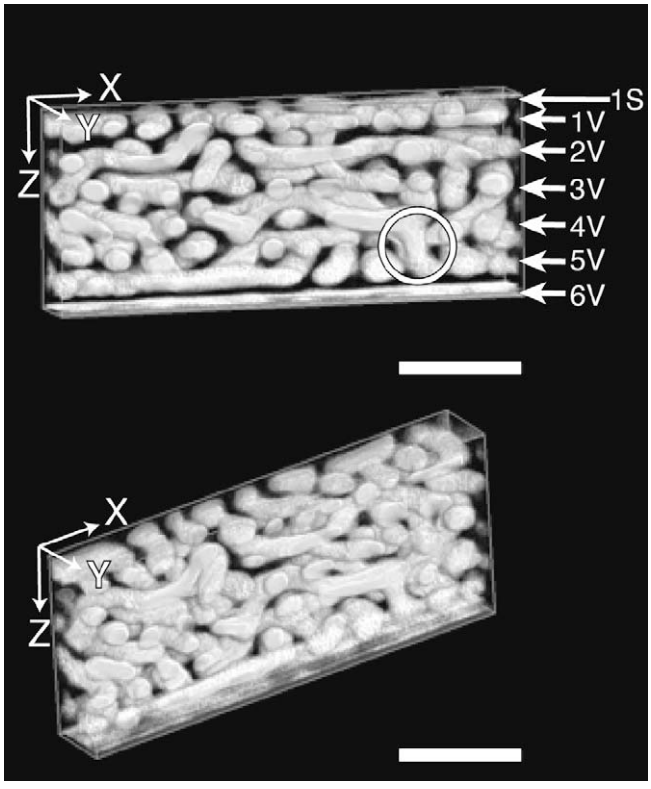

Fig. 25. Volume rendered 3D images of the dPS-*b*-P2VP thin film from two different viewpoints, in which the dPS microdomain was made transparent. The box size of each 3D image is $720 \times 90 \times 344$ nm. Arrows on the right of the 3D image indicate the P2VP layers. The 3D image was cropped along the *Y*-direction for viewing clarity (the total thickness in the *Y*-direction was 200 nm). Bar shows 200 nm. Reproduced with permission from Ref. [106]. Copyright 2007 American Chemical Society.

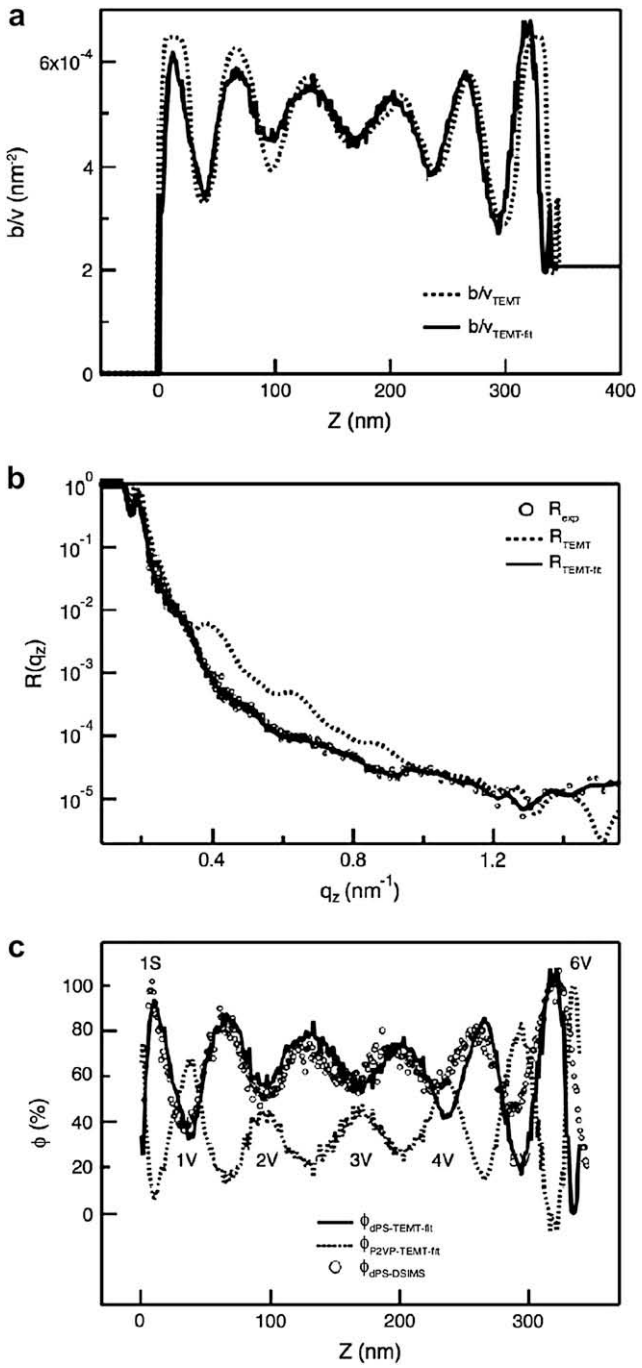

Fig. 26. (a) Scattering length density profile (b/v) of the dPS-*b*-P2VP. The dashed line is the calculated b/v profile from the 3D image obtained by TEMT. The solid line shown in part (b) is the calculated b/v profile from the best-fit reflectivity profile. (b) Reflectivity profile of the dPS-*b*-P2VP thin film. Open circles are the measured NR profile. The dashed line and the solid line represent the calculated reflectivity profile from the initial model obtained by TEMT and the best-fit reflectivity profile, respectively. (c) The concentration profiles of the dPS-*b*-P2VP thin film, ϕ. The solid and dashed lines correspond to the concentration of dPS and P2VP, respectively. Letters on the peaks of ϕ are used to specify the layers of dPS or P2VP where S and V denote dPS and P2VP, respectively. Open circles are the measured concentration profile of dPS by DSIMS. Reproduced with permission from Ref. [106]. Copyright 2007 American Chemical Society.

Fig. 26, which are shown, respectively, by the solid and dashed lines in Fig. 26(c). Alternatively, the concentration profile of dPS was estimated *independently* from the TEMT and NR using Dynamic secondary ion mass spectroscopy (DSIMS), $\phi_{\text{dPS-DSIMS}}$ [see the open circles in Fig. 26(c)]. $\phi_{\text{dPS-DSIMS}}$ showed excellent agreement with $\phi_{\text{dPS-TEMT-fit}}$, clearly demonstrating that the new methodology combining TEMT and NR provides not only a high resolution (through NR), but also an intuitive (through TEMT) way of characterizing the block copolymer morphologies. Detailed morphological discussion using the TEMT and NR data can be found elsewhere [106].

The novel methodology proposed here can be extended to the structural studies of the block copolymer thin film with more complicated and disordered morphologies, e.g., the gyroid, perforated layer, etc. We emphasize that the reflectivity alone had difficulty in dealing with these morphologies. In addition, the proposed methodology may also be extended to the off-specular scattering data [120,124–127] as well as specular scattering data, i.e., the reflectivity because the 3D volume data obtainable from TEMT provides not only the depth but also in-plane structural information.

6. Concluding remarks

This feature article summarizes recent advances in TEMT and its applications to polymer-related materials. With the dual-axis tomography and ultimately with full-rotation of the rod-shaped specimen ($\pm 90^\circ$ tilt), it is now possible to obtain *truly* quantitative 3D data in sub-nanometer resolution. Moreover, 3D imaging under stretching of a rubber composite (Si nano-particles in a rubbery matrix) has been successfully carried out [101]. It would be ideal if one could observe structural changes upon external stimuli, e.g., stretching, in 3D at the same volume of the specimen. In fact, although only 2D, "in situ" observations under special conditions, e.g., in high pressure, in high temperature, upon applying force, etc., are coming into fashion in the electron microscopy, especially in the field of metals. A special TEM holder that has AFM capability for simultaneous force measurement and imaging is now available. It can be easily imagined that all those TEM techniques will eventually go to 3D, which should be extremely beneficial to polymer morphological research.

Image contrast and electron beam damage on soft materials in TEMT experiments are always problems in polymer morphological studies. Staining with inorganic metals, e.g., OsO_4 and RuO_4, has often been used for the former problem and cryogenic TEM may be the solution for the latter. Phase-contrast TEM is proven to be quite useful to enhance the image contrast [128], which could be a new solution for the contrast enhancement. These TEM techniques shall be used together with CT in the biology field as well as in polymer research.

In some cases, structural elements on the order of sub-micrometer are responsible for materials properties. Moreover, most of the polymer morphologies are hierarchical. However, the maximum thickness of the specimen observable under TEMT is normally limited to ca. 300 nm in the case of the 200 kV TEM, which is too thin for the sub-micrometer structures. On the other hand, LSCM and X-ray CT do not provide such high resolution (their resolution is slightly less than 1 μm, at most). 3D imaging in sub-micrometer scale is still the missing zone. It is therefore necessary to develop new instruments that are capable of filling this resolution gap. The scanning electron microscopy combined with a focused ion beam (FIB-SEM) [129,130], high-resolution X-ray tomography system with focusing optics and scanning transmission electron microscopy (STEM) may be the candidates for this purpose. Of course, the existing TEM with very high voltage of 1 MV or more is an ideal instrument for thick samples but accessibility to such an instrument is somehow limited. STEM with better optics, optimized not for the ultra-high resolution but for the thick

samples, is eagerly anticipated. The fourth dimension, time, should be added to the 3D microscopy in the future.

From the 3D volume data obtainable by TEMT (and other 3D microscopy), some basic structural parameters, e.g., volume fraction of one of the constituents and interfacial area per unit volume, can be directly and relatively easily measured. These structural parameters are basic, but they are so far inferred from the 2D images and thus are possibly inaccurate. Characteristic length, being readily measured by use of scattering techniques, is also estimated by taking a Fourier Transform of the 3D images. Crystallographic analysis from the 3D images can be done with at least similar precision to the scattering, sometimes better than the scattering when a single grain can be obtained (Note that multiple grains in laser, X-ray and/or neutron beam smear the scattering pattern and accordingly ruin the spot-like pattern).

Although it would be useful enough for experimentalists to measure the above rather basic structural parameters from the 3D volume data, those are just a small advantage. The 3D digital data contains rich structural information and it can be extracted with the aid of "cutting-edge" quantitative image analysis. It is possible to go farther to evaluate a new set of parameters. Interfacial curvatures described in Section 4.3 are such examples. Connectivity of network domains of the morphologies is likewise important [80,131]. We would like to emphasize that those structural parameters have never been evaluated by any other (conventional) experimental techniques besides 3D microscopy. Thus, 3D microscopy together with the 3D digital analysis has great potential for analyzing polymer structures, and we hope that the methodology will unveil hidden physics in polymer science and open up new research areas in the future.

Acknowledgment

HJ is grateful to New Energy and Industrial Technology Develop Organization (NEDO) for support through the Japanese National Project "Nano-Structured Polymer Project" by the Ministry of Economy, Trade and Industry. Support given by the Grants-in-Aid No. 19031016 from the Ministry of Education, Science, Sports, Culture, Japan is also gratefully acknowledged.

References

[1] Gunton JD, Miguel MS, Sahni PS. In: Domb C, Lebowitz JL, editors. Phase transition and critical phenomena, vol. 8. New York: Academic Press; 1983. p. 269.
[2] Hashimoto T. Structure of polymer blends. In: Cahn RW, Haasen P, Kramer EJ, editors. Structure and properties of polymers. Materials science and technology, vol. 12. Weinheim: VCH; 1993. p. 251.
[3] Bates FS, Fredrickson GH. Phys Today 1999;52:32.
[4] Jinnai H, Nishikawa Y, Koga T, Hashimoto T. Macromolecules 1995;28:4782–4.
[5] Jinnai H, Koga T, Nishikawa Y, Hashimoto T, Hyde ST. Phys Rev Lett 1997; 78:2248–51.
[6] Jinnai H, Nishikawa Y, Morimoto H, Koga T, Hashimoto T. Langmuir 2000; 16:4380–93.
[7] Miller MK. Atom-probe tomography: analysis at the atomic level. New York: Kruwer Academic/Plenum Press; 2000.
[8] Spontak RJ, Williams MC, Agard DA. Polymer 1988;29:387–95.
[9] Kawase N, Kato M, Nishioka H, Jinnai H. Ultramicroscopy 2007;107:8–15.
[10] Ito T, Matsuwaki U, Otsuka Y, Katagiri G, Kato M, Matsubara K, et al. In: Vielstich W, Gasteiger HA, Yokokawa H, editors. Handbook of fuel cells, vol. 5. New Jersey: John Wiley & Sons; 2009.
[11] Bracewell RN. Aust J Phys 1956;9:297.
[12] Cormack AM. J Appl Phys 1963;34(9):2722.
[13] Hounsfield GN. A method and apparatus for examination of a body by radiation such as X or gamma radiation. The Patent Office, London, England; 1972.
[14] Rosier DJd, Klug A. Nature 1968;217:130.
[15] Hoppe W, Langer R, Knesch G, Poppe C. Naturwissenschaften 1968;55:333.
[16] Hart RG. Science 1968;159:1464.
[17] Crowther RA, DeRosier DJ, Klug A. Proc R Soc London 1970;A317:319–40.
[18] Vainshtein BK. Sov Phys Crystallogr 1970;15(5):781.
[19] Ramachandran GN, Lakshminarayanan AV. Proc Natl Acad Sci U S A 1971; 68(9):2236.
[20] Gordon R, Bender R, Herman GT. J Theor Biol 1970;29:471.
[21] Gilbert P. J Theor Biol 1972;36:105.
[22] Koster AJ, Grimm R, Typke D, Hegrel R, Stoschek A, Walz J, et al. J Struct Biol 1997;120:276.
[23] Radon J. Ber Verh K Sachs Ges Wiss Leipzig Math Phys Kl 1917;69:262.
[24] Cramer H, Wold H. J London Math Soc 1936;11:290.
[25] Thomas VM. In: Chisholm MH, editor. Inorganic chemistry: towards the 21st century, vol. 211. ACS Publication; 1983. p. 445.
[26] Deans SR. The radon transform and some of its applications. New York, Chichester: Wiley; 1983.
[27] Smith PR, Peters TM, Bates RHT. J Phys A Math Nucl Gen 1973;6:361.
[28] Radermacher M. Weighted back-projection methods. In: Frank J, editor. Electron tomography. New York: Plenum Press; 1992.
[29] Herman GT. Image reconstruction from projections. The fundamentals of computerized tomography. New York: Academic Press; 1980.
[30] Gilbert PFC. Proc R Soc London 1972;B182:89–102.
[31] Bates RHT, McDonnell MJ. Image restoration and reconstruction. New York: Oxford University Press; 1986.
[32] Frank J. Electron tomography: three-dimensional imaging with the transmission electron microscope. New York: Plenum; 1992.
[33] Midgley PA, Weyland M. Ultramicroscopy 2003;96:413.
[34] Jinnai H, Nishikawa Y, Ikehara T, Nishi T. Adv Polym Sci 2004;170:115–67.
[35] Sugimori H, Nishi T, Jinnai H. Macromolecules 2005;38:10226–33.
[36] Penczek P, Marko M, Buttle K, Frank J. Ultramicroscopy 1995;60:393–410.
[37] Mastronarde DN. J Struct Biol 1997;120:343–52.
[38] Lorensen WE, Cline HE. Computer graphics, SIGGRAPH '87, vol. 21; 1987. p. 163–9.
[39] Niihara K, Kaneko T, Suzuki T, Sato Y, Nishioka H, Nishikawa Y, et al. Macromolecules 2005;38:3048–50.
[40] Kaneko T, Nishioka H, Nishi T, Jinnai H. J Electron Microsc 2005;54:437–44.
[41] Radzilowski LH, Carragher BO, Stupp SI. Macromolecules 1997;30:2110–9.
[42] Jinnai H, Nishikawa Y, Spontak RJ, Smith SD, Agard DA, Hashimoto T. Phys Rev Lett 2000;84:518–21.
[43] Yamauchi K, Takahashi K, Hasegawa H, Iatrou H, Hadjichristidis N, Kaneko T, et al. Macromolecules 2003;36:6962–6.
[44] Wilder EA, Braunfeld MB, Jinnai H, Hall CK, Agard DA, Spontak RJ. J Phys Chem B 2003;107:11633–42.
[45] Nishioka H, Niihara K, Kaneko T, Yamanaka J, Inoue T, Nishi T, et al. Compos Interfaces 2006;13:589–603.
[46] Jinnai H, Shinbori Y, Kitaoka T, Akutagawa K, Mashita N, Nishi T. Macromolecules 2007;40:6758–64.
[47]. Kawasumi M, Hasegawa N, Kato M, Usuki A, Okada A. Macromolecules 1997;30:6333–8.
[48] Maiti P, Nam PH, Okamoto M, Hasegawa N, Usuki A. Macromolecules 2002;35:2042–9.
[49] Busfield JJC, Deeprasertkul C, Thomas AG. Polymer 2000;41:9219–25.
[50] Tsunoda K, Busfield JJC, Davies CKL, Thomas AG. J Mater Sci 2000;35: 5187–98.
[51] Yamaguchi K, Busfield JJC, Thomas AG. J Polym Sci Part B Polym Phys 2003;41:2079–167.
[52] Busfield JJC, Thomas AG, Yamaguchi K. J Polym Sci Part B Polym Phys 2003;42:2897–903.
[53] Yu J, Lu K, Sourty E, Grossiord N, Koning CE, Loos J. Carbon 2007;45:2897–903.
[54] Bavel SSv, Sourty E, With Gd, Loos J. Nano Lett, in press. doi:10.1021/nl8014022.
[55] Drummy LF, Wang YC, Schoenmakers R, May K, Jackson M, Koerner H, et al. Macromolecules 2008;41:2135–43.
[56] Guth E. J Appl Phys 1945;16:20–5.
[57] Siegfried W, Degussa A. Rubber Chem Technol 1996;69:325–46.
[58] Karasek L, Sumita M. J Mater Sci 1996;31:281–9.
[59] Egerton RF. Electron energy-loss spectroscopy in the electron microscope. New York: Plenum; 1996.
[61] Hon AA, Busfield JJC, Thomas AG. Constitutive models for rubber III. London: Balkema; 2003. p. 301–8.
[62] Akutagawa K, Yamaguchi K, Yamamoto A, Heguri H, Jinnai H, Shinbori Y. Rubber Chem Technol 2008;81(2):182–9.
[63] Tchoudakov R, Breuer O, Narkis M, Siegmann A. Polym Eng Sci 1996; 36:1336–46.
[64] Lim YT, Park OO. Macromol Rapid Commun 2001;21:231–5.
[65] Ray SS, Okamoto K, Okamoto M. Macromolecules 2003;36:2355–67.
[66] Giannelis EP. Adv Mater 1996;8:29–35.
[67] Goldstein H. Classical mechanics. Reading: Addison Wesley; 1950.
[68] Spontak RJ, Fung JC, Braunfeld MB, Sedat JW, Agard DA, Kane L, et al. Macromolecules 1996;29:4494–507.
[69] Laurer JH, Hajduk DA, Fung JC, Sedat JW, Smith SD, Gruner SM, et al. Macromolecules 1997;30:3938–41.
[70] Jinnai H, Nishikawa Y, Ito M, Smith SD, Agard DA, Spontak RJ. Adv Mater 2002;14:1615–8.
[71] Xu T, Zvelindovsky AV, Sevink GJA, Lyakhova KS, Jinnai H, Russell TP. Macromolecules 2005;38:10788–98.
[72] Jinnai H, Sawa K, Nishi T. Macromolecules 2006;39:5815–9.
[73] Jinnai H, Hasegawa H, Nishikawa Y, Sevink GJA, Braunfeld MB, Agard DA, et al. Macromol Rapid Commun 2006;27:1424–9.
[74] Jinnai H, Yasuda K, Nishi T. Macromol Symp 2006;245–246:170–4.

[75] Kaneko T, Suda K, Satoh K, Kamigaito M, Kato T, Ono T, et al. Macromol Symp 2006;242:80–6.
[76] Park HW, Im K, Chung B, Ree M, Chang T, Sawa K, et al. Macromolecules 2007;40:2603–5.
[77] Miura Y, Kaneko T, Satoh K, Kamigaito M, Jinnai H, Okamoto Y. Chem Asian J 2007;2:662–72.
[78] Chen Y, Du J, Xiong M, Guo H, Jinnai H, Kaneko T. Macromolecules 2007;40:4389–92.
[79] Yang X, Loos J. Macromolecules 2007;40:1353–62.
[80] Jinnai H, Kajihara T, Watashiba H, Nishikawa Y, Spontak RJ. Phys Rev E 2001;64: 010803(R)–010806(R), 069903(E).
[81] Abetz V, Simon PFW. Adv Polym Sci 2005;189:125–212.
[82] Thomas EL, Alward DB, Kinning DJ, Martin DC, Handlin Jr DL, et al. Macromolecules 1986;19:2197–202.
[83] Thomas EL, Anderson DM, Henkee CS, Hoffman D. Nature 1988;334:598–601.
[84] Schulz ML, Bates FS, Almdal K, Mortensen K. Phys Rev Lett 1994;73:86–9.
[85] Hajduk DA, Harper PE, Gruner SM, Honeker CC, Kim G, Thomas EL, et al. Macromolecules 1994;27:4063–75.
[86] Hajduk DA, Ho RM, Hillmyer MA, Bates FS, Almdal K. J Phys Chem B 1998; 102:1356–63.
[87] Schick M. Physica A 1998;251:1–11.
[88] Hajduk DA, Harper PE, Gruner SM, Honeker CC, Thomas EL, Fetters LJ. Macromolecules 1995;28:2570–3.
[89] Hyde ST, Andersson S, Larsson K, Blum Z, Landh T, Lidin S, et al. The language of shape. Amsterdam: Elsevier Science B.V.; 1997.
[90] Matsen MW, Bates FS. Macromolecules 1996;29:7641–4.
[91] Matsen MW, Bates FS. J Chem Phys 1997;106:2436–48.
[92] Gruner SM. J Phys Chem 1989;93:7562–70.
[93] Fung JC, Liu W, deRuijter WJ, Chen H, Abbey CK, Sedat JW, et al. J Struct Biol 1996;116:181s–9s.
[94] Frank J. Principles of electron tomography. New York: Plenum Press; 1992. p. 1–16.
[95] Nishikawa Y, Jinnai H, Koga T, Hashimoto T. Langmuir 2001;17:3254–65.
[96] Ehlich D, Takenaka M, Okamoto S, Hashimoto T. Macromolecules 1993;26:189–97.
[97] Ehlich D, Takenaka M, Hashimoto T. Macromolecules 1993;26:492–8.
[98] Nishikawa Y, Kawada H, Hasegawa H, Hashimoto T. Acta Polym 1993;44: 247–55.
[99] Gido SP, Gunther J, Thomas EL, Hoffman D. Macromolecules 1993;26: 4506–20.
[100] Gido SP, Thomas EL. Macromolecules 1994;27:849–61.
[101] Dohi H, Kimura H, Kotani M, Kaneko T, Kitaoka T, Nishi T, et al. Polym J 2007;39:749–58.
[102] Mareau VH, Akasaka S, Osaka T, Hasegawa H. Macromolecules 2007; 40:9032–9.
[103] Jinnai H, Sawa K, Hirato F, Park HW, Jung J, Lee S, et al., in preparation.
[104] Sugimori H, Niihara K, Kaneko T, Miyoshi W, Jinnai H. Prog Theor Phys Suppl 2008;175:166–73.
[105] Morita H, Kawakatsu T, Doi M, Nishi T, Jinnai H. Macromolecules 2008;41:4845–49.
[106] Niihara K, Matsuwaki U, Torikai N, Atarashi H, Tanaka K, Jinnai H. Macromolecules 2007;40:6940–6.
[107] Fasolka MJ, Mayes AM. Ann Rev Mater Res 2001;31:323--55.
[108] Russell TP. Physica B 1996;221:267–83.
[109] Guarini KW, Black CT, Zhang Y, Kim H, Sikorski EM, Babich IV. J Vac Sci Technol B 2002;20:2788–92.
[110] Hamley IW. Nanotechnology 2003;14:R39–54.
[111] Park C, Yoon J, Thomas EL. Polymer 2003;44:6725–60.
[112] Stoykovich MP, Muller M, Kim S, Solak HH, Edwards EW, Pablo JJ, et al. Science 2005;308:1442–6.
[113] Widawski G, Rawiso M, François B. Nature 1994;369:387–9.
[114] Freer EM, Krupp LE, Hinsberg WD, Rice PM, Hedrick JL, Cha JN, et al. Nano Lett 2005;5:2014–8.
[115] Kenneth R, Russell TP. Macromolecules 1993;26:1047–52.
[116] Mayes AM, Russell TP. Macromolecules 1993;26:3929–36.
[117] Torikai N, Noda I, Karim A, Satija SK, Han CC, Matsushita Y, et al. Macromolecules 1997;30:2907–14.
[118] Noro A, Okuda M, Odamaki F, Kawaguchi D, Torikai N, Takano A, et al. Macromolecules 2006;39:7654–61.
[119] Parratt LG. Phys Rev 1954;95:359–69.
[120] Russell TP. Mater Sci Rep 1990;5:171–271.
[121] Karim A, Guo L, Rafailovichi MH, Sokolov J, Peiffer DG, Schwarz SA, et al. J Chem Phys 1994;100:1620–9.
[122] Ge S, Guo L, Colby RH, Dozier WD. Langmuir 1999;15:2911–5.
[123] Knoll A, Tsarkova L, Krausch G. Nano Lett 2007;7:843–6.
[124] Pasyuk VL, Lauter HJ, Gordeev GP, Buschbaum PM, Toperverg BP, Jernenkov M, et al. Langmuir 2003;19:7783–8.
[125] Lee B, Park I, Yoon J, Park S, Kim J, Kim K, et al. Macromolecules 2005;38:4311–23.
[126] Wang J, Leiston-Belanger JM, Sievert JD, Russell TP. Macromolecules 2006;39:8487–91.
[127] Buschbaum PM, Maurer E, Bauer E, Cabitt R. Langmuir 2006;22:9295–303.
[128] Tosaka M, Danev R, Nagayama K. Macromolecules 2005;38:7884–6.
[129] Wilson JR, Kobsiriphat W, Mendoza R, Chen HY, Hiller JM, Miller DJ, et al. Nat Mater 2006;5:541–4.
[130] Kato M, Ito T, Aoyama Y, Sawa K, Kaneko T, Kawase N, et al. J Polym Sci Part B Polym Phys 2007;45:677–83.
[131] Jinnai H, Watashiba H, Kajihara T, Takahashi M. J Chem Phys 2003;119: 7554–9.

Hiroshi Jinnai was born in Osaka, Japan, in 1965, and graduated from the Department of Polymer Chemistry of Kyoto University, Kyoto, Japan in 1988. He studied polymer physics and was awarded a Doctor of Engineering in 1993. During this period, he was a guest scientist twice at National Institute of Standards and Technology (Gaithersburg, Maryland) from 1988 to 1989 and from 1991 to 1992. He received a Japan Society for the Promotion of Science Research Fellowship for Young Scientists in 1993. In 1993, he joined an Exploratory Research for Advanced Technology program, Hashimoto Polymer Phasing Project, as a group leader. He was appointed as lecturer at Kyoto Institute of Technology in 1998 and was promoted to associate professor in 2002.In 2006, he was awarded the The Society of Polymer Science, Japan (SPSJ) Wiley Award for his three-dimensional (3D) structural studies of phase-separation and self-assembling processes of polymer systems.In 2007, he became the first Japanese ever to win the prestigious biannual Ernst Ruska Award with Professor Richard J. Spontak of North Carolina State University, USA and Professor Paul A. Midgley of University of Cambridge, United Kingdom. This award, named after Ernst Ruska, winner of the 1986 Nobel Prize for his invention of the transmission electron microscope, is given by the Deutsche Gesellschaft fur Elektronenmikroskopie (German Society of Electron Microscopy). Their joint study entitled "Novel and Quantitative Uses of Electron Tomography in the 3D Study of Nano-structured Materials" made possible the observation of three-dimensional objects less than 1 nm. In 2008, he received award for Persons of Merit in Industry-Academia-Government Collaboration in FY2008 (Minister of Education, Culture, Sports, Science and Technology Award) again for the development of Electron Tomography.His research interests are the self-assembling morphologies and processes of polymer blends and block copolymers. He is also a recognized world expert in 3D visualization of soft-condensed matters.